

Electrostatic potential variations on stellarator magnetic surfaces in low collisionality regimes

Iván Calvo¹, José Luis Velasco¹, Félix I. Parra^{2,3}, J. Arturo Alonso¹
and José Manuel García-Regaña¹

¹Laboratorio Nacional de Fusión, CIEMAT, 28040 Madrid, Spain

²Rudolf Peierls Centre for Theoretical Physics, University of Oxford, Oxford, OX1 3PU, UK

³Culham Centre for Fusion Energy, Abingdon, OX14 3DB, UK

(Received 22 August 2018)

The component of the neoclassical electrostatic potential that is non-constant on the magnetic surface, that we denote by $\tilde{\varphi}$, can affect radial transport of highly charged impurities, and this has motivated its inclusion in some modern neoclassical codes. The number of neoclassical simulations in which $\tilde{\varphi}$ is calculated is still scarce, partly because they are usually demanding in terms of computational resources, especially at low collisionality. In this paper the size, the scaling with collisionality and with aspect ratio, and the structure of $\tilde{\varphi}$ on the magnetic surface are analytically derived in the $1/\nu$, $\sqrt{\nu}$ and superbanana-plateau regimes of stellarators close to omnigenity; i. e. stellarators that have been optimized for neoclassical transport. It is found that the largest $\tilde{\varphi}$ that the neoclassical equations admit scales linearly with the inverse aspect ratio and with the size of the deviation from omnigenity. Using a model for a perturbed omnigenous configuration, the analytical results are verified and illustrated with calculations by the code KNOSOS. The techniques, results and numerical tools employed in this paper can be applied to neoclassical transport problems in tokamaks with broken axisymmetry.

1. Introduction

The transport of impurities in three-dimensional toroidal magnetic fields has attracted much attention from the stellarator community. In stellarators, the accumulation of impurities in the center of the confinement region often limits the discharge duration and is considered to be a potential problem for the development of future reactors. In the framework of neoclassical theory, this accumulation has generally been explained with the inward convection caused by the typically negative radial electric field acting on the highly charged ions in the absence of a so-called “temperature screening” effect in non-axisymmetric systems[†]. In a qualitative sense, these expectations are consistent with the general trend observed in the impurity confinement time (Burhenn *et al.* 2009), although there are remarkable experimental observations of outward impurity transport (see, for example, McCormick *et al.* (2002); Ida *et al.* (2009)). This outward impurity flux is still poorly understood. On a quantitative level, it is difficult to determine whether the observed impurity fluxes agree with calculations relying on the solution of approximate versions of the drift-kinetic equation, for these comparisons are often fragmented, dealing with a reduced number of plasma profiles and based on different measuring techniques.

[†] Recently, both the prevalence of the radial electric field in the transport of impurities and the absence of impurity screening in three-dimensional magnetic fields have been brought into question for several collisionality regimes (Velasco *et al.* 2017; Helander *et al.* 2017).

The fundamental output of neoclassical modeling of impurity transport is the spatially resolved radial particle flux of a charge state of a certain impurity species, and it is often the case that this very quantity is not experimentally accessible, which complicates the direct quantitative comparisons.

The kinetic modeling of impurity dynamics and transport has undergone recent improvements with the inclusion of terms that had previously been considered of secondary importance (García-Regaña *et al.* 2013). These terms model the modification of the trajectories of impurity ions by the component of the electrostatic potential that is non-constant on the flux surface, that we denote by $\tilde{\varphi}$ and that defines the component of the electric field that is tangent to the flux surface. Specifically, this tangential electric field produces a radial $E \times B$ drift that advects impurities on the flux surface. The effect of $\tilde{\varphi}$ on impurity transport is larger for impurities with higher electric charge.

A previous step to the assessment of the impact of $\tilde{\varphi}$ on radial impurity transport is the neoclassical calculation of $\tilde{\varphi}$ itself[†], which has typically been ignored in standard neoclassical simulations. The modern codes EUTERPE (Kornilov *et al.* 2005) and SFINCS (Landreman *et al.* 2014) can compute it. In García-Regaña *et al.* (2017), results of $\tilde{\varphi}$ from both codes for different stellarators and plasma regimes are presented. These extended neoclassical models have started to be used to revisit some of the previous calculations of neoclassical impurity fluxes and have shown substantial deviations (with respect to codes that do not include the effect of $\tilde{\varphi}$) for some machines and plasma conditions (García-Regaña *et al.* 2017; Mollén *et al.* 2018). Recently, the strong effect of $\tilde{\varphi}$ on the neoclassical transport of highly charged collisional impurities in stellarators has been analytically proven in (Calvo *et al.* 2018).

Given the relevance of correctly determining $\tilde{\varphi}$, it is important to understand the equations that have to be solved to calculate it, and to derive and discuss analytically some features of the solutions to these equations. In this paper we do so for main ions in the $1/\nu$, $\sqrt{\nu}$ and superbanana-plateau low collisionality regimes (see Mynick (1984) for estimations of the effect of $\tilde{\varphi}$ on main ion transport in low collisionality regimes under some simplified assumptions). Low collisionality regimes are the pertinent ones for the main ions in the core of reactor-relevant stellarator plasmas and, in addition, in these regimes $\tilde{\varphi}$ is large and has significant impact on impurity transport. We will carry out such analytical discussion by using the techniques and results of Calvo *et al.* (2017), where we studied the radial neoclassical transport of low collisionality ions in stellarators close to omnigenity. Omnigenous magnetic fields (Hall & McNamara 1975; Cary & Shasharina 1997; Parra *et al.* 2015) are those for which the orbit-averaged radial magnetic drift vanishes for all trapped particles. Omnigenous stellarators can be said to be perfectly optimized from a neoclassical point of view, exhibiting transport levels similar to those of a tokamak. In Calvo *et al.* (2017), expansions in large aspect ratio were not considered. In this article, we expand in small inverse aspect ratio (in the end, all stellarators in operation today have large aspect ratio (Beidler *et al.* 2011)). We will see that the large aspect ratio expansion introduces a number of subtleties.

Let us emphasize that closeness to omnigenity is not a mere academic requirement. It is well-known (Galeev & Sagdeev 1979; Ho & Kulsrud 1987) that, for sufficiently low ion collisionality, tangential drifts have to be kept in the stellarator drift-kinetic equation. If the radial electric field is not small and the aspect ratio is large, one can show that the drift-kinetic equation is radially local and that the tangential magnetic drift

[†] As a matter of fact, this has brought up the relevance of the measurement of $\tilde{\varphi}$ (Pedrosa *et al.* 2015) and its impact on impurity density inhomogeneities (Arévalo *et al.* 2014; Alonso *et al.* 2016).

is negligible compared to the tangential $E \times B$ drift. But if one of these assumptions fails (that is, if the radial electric field is small or the stellarator is compact), the drift-kinetic equation becomes radially global (with obvious negative consequences for confinement, because then the radial excursion associated with a particle orbit can be as large as the stellarator minor radius) at small collisionality values unless the stellarator is close to omnigenity. If the magnetic configuration is close to being omnigeneous and the deviation from omnigenity has small spatial gradients, the set of equations consisting of the drift-kinetic equation and the quasineutrality equation can be rigorously proven to be linear and radially local (Calvo *et al.* 2017). Not only do the resulting equations include the effect of $\tilde{\varphi}$, but also the effect of the tangential magnetic drift. As we have pointed out, the tangential magnetic drift has to be taken into account to describe the transport of the main ions at very low collisionality in compact stellarators and in situations of small radial electric field even if the aspect ratio is large. The importance of the tangential magnetic drift in the latter case is a subject of active research (Matsuoka *et al.* 2015). In this paper, we will pay special attention to the behavior of $\tilde{\varphi}$ in regimes where the tangential magnetic drift has to be retained.

Apart from discussing $\tilde{\varphi}$ analytically in the $1/\nu$, $\sqrt{\nu}$ or superbanana-plateau regimes, we will verify and illustrate the results by comparing them with KNOSOS (Velasco *et al.* 2018), a newly developed bounce-averaged code that solves the drift-kinetic and quasineutrality equations derived in Calvo *et al.* (2017) (for the time being, KNOSOS uses a pitch-angle scattering collision operator), and therefore retains the tangential magnetic drift (among the two codes mentioned some paragraphs above, EUTERPE does not retain the tangential magnetic drift, whereas a way to try to retain it in SFINCS has been recently reported in Paul *et al.* (2017)). Finally, a remark on the scope of this paper is in order. Whereas the expansion around omnigenity should be considered as a realistic approach to the analysis of magnetic configurations that aspire to confine sufficiently well to be the basis of stellarator reactor designs, our present treatment is limited by the requirement of small gradients of the non-omnigeneous perturbation in Calvo *et al.* (2017). It would be important to address the relaxation of this condition in future research. Some ideas about the kind of complications introduced by large gradients can be found in Calvo *et al.* (2014, 2015) in the setting of perturbed quasisymmetric configurations. Stellarators close to quasisymmetry where the non-quasisymmetric perturbation has small gradients were treated in detail in Calvo *et al.* (2013). Finally, we note that a tokamak with (slightly) broken axisymmetry can be viewed as a particular case of a magnetic configuration close to omnigenity, and therefore the tools and results of this paper can be directly applied to problems such as the calculation of tokamak neoclassical toroidal viscosity.

The rest of the paper is organized as follows. In Section 2, after defining the coordinates that will be employed in the theoretical derivations (subsection 2.1) and introducing the notion of omnigenity (subsection 2.2), we present in subsection 2.3 the neoclassical equations that determine $\tilde{\varphi}$ in low collisionality regimes of stellarators close to omnigenity when the deviation from omnigenity has small spatial gradients. We will also see how $\tilde{\varphi}$ scales with the size of the deviation from omnigenity. In subsection 2.4, and for large aspect ratio, the scaling with aspect ratio of some quantities entering the neoclassical equations is given; these expressions will be useful in later sections. In subsection 2.5, the magnetic field close to omnigenity that we will use for the numerical examples is described. With this magnetic field, and taking reactor-relevant parameter values, in Section 3 we give a plot (see figure 3) calculated by KNOSOS showing the dependence of the size of the non-constant component of the electrostatic potential on the collisionality and the radial electric field. The objective of the next section, Section 4, is to explain mathematically the different regimes observed in plots like that in figure 3. Hence, in Section 4

we discuss analytically the features of $\tilde{\varphi}$ in the $1/\nu$, $\sqrt{\nu}$ and superbanana-plateau asymptotic regimes as implied by the equations given in subsection 2.3 (as explained in Calvo *et al.* (2017), those equations are not valid for lower collisionality regimes like the superbanana or ν regimes, the essential reason being that for such low collisionality values one has to take into account the radial displacement of the trajectories). In particular, we will comment on the scaling of $\tilde{\varphi}$ with collisionality and aspect ratio, as well as on its behavior under stellarator symmetry transformations. Detailed numerical checks of the analytical results with KNOSOS are provided throughout this section. Of course, assuming closeness to omnigenity is not required if one is only interested in studying the $1/\nu$ and $\sqrt{\nu}$ regimes (the former exists in any stellarator and the latter exists in large aspect ratio stellarators with non-small radial electric field), but the assumption is necessary to be able to study, in the same framework, those two collisionality regimes together with the superbanana-plateau regime. In Section 5, we give the conclusions. In particular, table 1 condenses the main analytical results derived in the paper. Finally, we point out that, for simplicity, throughout the paper we assume that the electrons are adiabatic. This is a good approximation in many cases, but its accuracy certainly depends on the particular collisionality regimes in which the main ions and the electrons are, and situations in which the electrons have to be treated kinetically are not uncommon (see, e.g. Velasco *et al.* (2017); García-Regaña *et al.* (2018)). In these situations, a kinetic treatment of the electrons is also needed to calculate $\tilde{\varphi}$.

2. Low collisionality neoclassical equations in stellarators close to omnigenity

2.1. Phase space coordinates

In the kinetic description of low collisionality regimes, it is useful to employ spatial coordinates $\{r, \alpha, l\}$, defined as follows. The radial coordinate $r \in [0, a]$ labels the magnetic surface and has dimensions of length, a being the minor radius of the stellarator. For given r , the angular coordinate $\alpha \in [0, 2\pi)$ selects a magnetic field line on the surface. The coordinate $l \in [0, l_{\max}(r, \alpha))$ is the arc length along the field line. In these coordinates the magnetic field reads

$$\mathbf{B} = \Psi(r)\nabla r \times \nabla\alpha. \quad (2.1)$$

As for the meaning of the flux function $\Psi(r)$, it is easy to check that $2\pi \int_0^{r_0} \Psi(r)dr$ equals the magnetic flux across a surface defined by $l = \text{const.}$ and $0 \leq r \leq r_0$.

In these coordinates the flux-surface average of a function $f(r, \alpha, l)$ is defined as

$$\langle f \rangle(r) = V'(r)^{-1} \int_0^{2\pi} d\alpha \int_0^{l_{\max}} dl \Psi B^{-1} f, \quad (2.2)$$

where $\Psi B^{-1} = [(\nabla r \times \nabla\alpha) \cdot \nabla l]^{-1}$ is the volume element (the coordinates $\{r, \alpha, l\}$ are chosen such that $\Psi > 0$), $B(r, \alpha, l)$ is the magnitude of \mathbf{B} and

$$V'(r) = \int_0^{2\pi} d\alpha \int_0^{l_{\max}} dl \Psi B^{-1}, \quad (2.3)$$

with $V(r)$ being the volume enclosed by the surface r . We will use primes to denote differentiation with respect to r .

In velocity space, we employ coordinates $\{v, \lambda, \sigma\}$, where v is the magnitude of the velocity \mathbf{v} , $\lambda = v_{\perp}^2/(Bv^2)$ is the pitch-angle coordinate, v_{\perp} is the component of \mathbf{v} per-

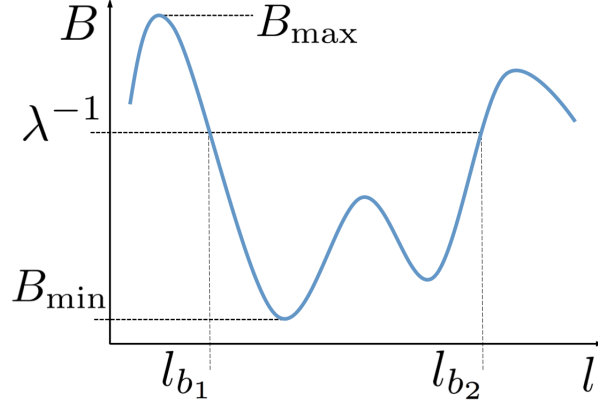


FIGURE 1. Cartoon showing some of the quantities (defined in the text) employed to describe a trapped trajectory.

pendicular to \mathbf{B} and $\sigma = v_{||}/|v_{||}|$ is the sign of the parallel velocity, with

$$v_{||}(r, \alpha, l, v, \lambda, \sigma) = \sigma v \sqrt{1 - \lambda B(r, \alpha, l)}. \quad (2.4)$$

Integrals over velocity space of gyrophase-independent functions (all functions in this paper are independent of gyrophase) read, in these coordinates,

$$\int (\cdot) d^3v \equiv \sum_{\sigma} \int_0^{\infty} dv \int_0^{B^{-1}} d\lambda \frac{\pi B v^3}{|v_{||}|} (\cdot). \quad (2.5)$$

2.2. Perturbed omnigenous magnetic fields

Trapped trajectories are those with $\lambda \in [B_{\max}^{-1}, B_{\min}^{-1}]$, where $B_{\max}(r)$ and $B_{\min}(r)$ are, respectively, the maximum and minimum values of B on the flux surface. For each trapped trajectory, the second adiabatic invariant reads

$$J(r, \alpha, v, \lambda) = 2 \int_{l_{b1}}^{l_{b2}} |v_{||}| dl. \quad (2.6)$$

Here, l_{b1} and l_{b2} are the bounce points of the trapped orbit, obtained by solving in l the equation $1 - \lambda B(r, \alpha, l) = 0$ (see figure 1 for a cartoon showing some of the quantities that describe trapped trajectories).

The importance of J comes from the relations

$$\frac{2}{\tau_b} \int_{l_{b1}}^{l_{b2}} \frac{1}{|v_{||}|} \mathbf{v}_M \cdot \nabla r dl = \frac{m}{Ze\Psi\tau_b} \partial_{\alpha} J, \quad (2.7)$$

$$\frac{2}{\tau_b} \int_{l_{b1}}^{l_{b2}} \frac{1}{|v_{||}|} \mathbf{v}_M \cdot \nabla \alpha dl = -\frac{m}{Ze\Psi\tau_b} \partial_r J, \quad (2.8)$$

where

$$\mathbf{v}_M = \frac{mv^2(1 - \lambda B)}{ZeB} \hat{\mathbf{b}} \times (\hat{\mathbf{b}} \cdot \nabla \hat{\mathbf{b}}) + \frac{mv^2\lambda}{2ZeB} \hat{\mathbf{b}} \times \nabla B \quad (2.9)$$

is the magnetic drift, $\hat{\mathbf{b}} = B^{-1}\mathbf{B}$, m is the particle mass, Ze is the particle charge (we assume $Z \sim 1$), e is the proton charge and

$$\tau_b(r, \alpha, v, \lambda) = 2 \int_{l_{b1}}^{l_{b2}} |v_{||}|^{-1} dl \quad (2.10)$$

is the bounce time; i.e. the time that the trapped particle needs to complete its orbit. Hence, $\partial_\alpha J$ and $\partial_r J$ contain the information on the motion of the trapped particle in the directions perpendicular to \mathbf{B} , averaged over the motion in the direction parallel to \mathbf{B} .

The magnetic field is called omnigeneous (Cary & Shasharina 1997; Parra *et al.* 2015) if the average radial magnetic drift vanishes for all trapped particles. Due to (2.7), this is equivalent to saying that the second adiabatic invariant is independent of α , $\partial_\alpha J = 0$, for all trapped trajectories.

From the definition of omnigeneity one can deduce that, for any function q that depends on α and l only through an omnigeneous magnetic field B , one has (Cary & Shasharina 1997; Helander & Nührenberg 2009; Calvo *et al.* 2017)

$$\partial_\alpha \int_{l_{b_1}}^{l_{b_2}} q(r, v, \lambda, B(r, \alpha, l)) dl = 0. \quad (2.11)$$

This useful property is employed in the derivation of the neoclassical equations of subsection 2.3 and it will also be used in the analysis of their solutions.

In this paper, we will carry out the calculations in magnetic configurations that can be written as an exactly omnigeneous magnetic field \mathbf{B}_0 plus a perturbation $\delta\mathbf{B}_1$,

$$\mathbf{B} = \mathbf{B}_0 + \delta\mathbf{B}_1, \quad (2.12)$$

where $B_0 := |\mathbf{B}_0| \sim |\mathbf{B}_1| =: B_1$ and $0 \leq \delta \ll 1$. As advanced in Section 1, and following Calvo *et al.* (2017), we restrict ourselves to cases in which the characteristic scale of variation of B_1 on the flux surface is not much smaller than that of B_0 . Specifically, we require $|\partial_\alpha B_1|/|\partial_\alpha B_0| \sim |\partial_l B_1|/|\partial_l B_0| \ll \delta^{-1}$. Thus, in terms of an expansion in $\delta \ll 1$, we can assume that B_0 and B_1 have a similar characteristic variation length on the flux surface, that we can take to be R_0 , the major radius of the stellarator. This is what we mean when we say that the deviation from omnigeneity has small gradients. In particular, deviations with small gradients can deform the omnigeneous magnetic wells, but not create new wells.

2.3. Drift-kinetic and quasineutrality equations in stellarators close to omnigeneity

In drift kinetics (Hazeltine 1973; Parra & Calvo 2011; Calvo *et al.* 2013), the characteristic frequency of particle motion in the direction parallel to \mathbf{B} is $O(v_t/R_0)$, whereas the motion perpendicular to the magnetic field has a much smaller typical frequency $O(\rho_* v_t/R_0)$, where $\rho_* = \rho/R_0 \ll 1$ is the normalized Larmor radius, with $\rho = v_t/\Omega$ and $\Omega = ZeB/m$. Low collisionality regimes[†] are defined by $\nu_* \ll 1$, where $\nu_* = \nu_{ii} R_0/v_t$ is the ion collisionality, ν_{ii} is the ion-ion collision frequency and $v_t = \sqrt{T/m}$ is the ion thermal speed. The condition $\nu_* \ll 1$ means that the characteristic parallel streaming frequency is much greater than the collision frequency ν_{ii} , and therefore the drift-kinetic ion equation can be averaged over the parallel motion. In this subsection, we give the neoclassical equations for low collisionality plasmas in stellarators close to omnigeneity where the deviation from omnigeneity has small gradients, but we do not include their derivation. For that, we refer the reader to Calvo *et al.* (2017). No assumptions are made about the aspect ratio of the stellarator yet.

For $\delta \ll 1$, one finds that the electrostatic potential, φ , is a flux function to lowest

[†] From here on, we understand that quantities without a subindex specifying the species refer to ions. Electron quantities will always include a subindex e . In some ion quantities where some ambiguity might exist, as in ν_{ii} , we include subindices.

order,

$$\varphi(r, \alpha, l) = \varphi_0(r) + \delta\varphi^{(1)}(r, \alpha, l) + \dots \quad (2.13)$$

The component of the electrostatic potential that is non-constant on the flux surface, denoted in Section 1 by $\tilde{\varphi}$, is therefore given by

$$\tilde{\varphi} = \varphi - \varphi_0 = \delta\varphi^{(1)} + \dots \quad (2.14)$$

In an expansion in δ , the ion distribution function, F , can be written as

$$F = F_M - \frac{Ze\delta\varphi^{(1)}}{T} F_M + \delta g^{(1)} + \dots, \quad (2.15)$$

where F_M is a Maxwellian distribution constant on flux surfaces,

$$F_M(r, v) = n(r) \left(\frac{m}{2\pi T(r)} \right)^{3/2} \exp \left(-\frac{mv^2}{2T(r)} \right), \quad (2.16)$$

and n and T are the ion density and temperature. The non-adiabatic perturbation to the Maxwellian distribution, $g^{(1)}(r, \alpha, l, v, \lambda)$, is independent of l and σ , and vanishes for passing trajectories of the omnigenous field, $0 \leq \lambda < B_{0,\max}^{-1}$, where $B_{0,\max}(r)$ is the maximum value of B_0 on the flux surface. The function $g^{(1)}$ can be chosen such that

$$\int_0^{2\pi} g^{(1)} d\alpha = 0. \quad (2.17)$$

The equations that determine $g^{(1)}$ and $\varphi^{(1)}$ are radially local and linear. First, one has the bounce-averaged drift-kinetic equation for trapped trajectories,

$$-\partial_r J^{(0)} \partial_\alpha g^{(1)} + \partial_\alpha J^{(1)} \Upsilon F_M = \sum_\sigma \frac{Ze\Psi}{m} \int_{l_{b10}}^{l_{b20}} \frac{1}{|v_{||}^{(0)}|} C_{ii}^{\ell(0)} [g^{(1)}] dl, \quad (2.18)$$

where[†]

$$\partial_r J^{(0)} = - \int_{l_{b10}}^{l_{b20}} \frac{\lambda v \partial_r B_0 + 2Ze/(mv) \varphi'_0}{\sqrt{1 - \lambda B_0}} dl, \quad (2.19)$$

$$J^{(1)} = - \int_{l_{b10}}^{l_{b20}} \frac{\lambda v B_1 + 2Ze/(mv) \varphi^{(1)}}{\sqrt{1 - \lambda B_0}} dl, \quad (2.20)$$

$$\Upsilon = \frac{n'}{n} + \frac{T'}{T} \left(\frac{mv^2}{2T} - \frac{3}{2} \right) + \frac{Ze\varphi'_0}{T} \quad (2.21)$$

and C_{ii}^ℓ is the linearized ion-ion collision operator (Helander & Sigmar 2002). The ion-electron collision term has been neglected because we assume $\sqrt{m_e/m} \ll 1$, with m_e the electron mass. The superindex (0) in $C_{ii}^{\ell(0)}$ means that B has been replaced by B_0 in the expression for the collision operator in coordinates v and λ . Analogously,

$$v_{||}^{(0)}(r, \alpha, l, v, \lambda, \sigma) = \sigma v \sqrt{1 - \lambda B_0(r, \alpha, l)}, \quad (2.22)$$

and l_{b10} , l_{b20} are the solutions of the equation $1 - \lambda B_0(r, \alpha, l) = 0$ for $\lambda \geq B_{0,\max}^{-1}$. Finally,

[†] The presence of φ in the expressions for $\partial_r J^{(0)}$ and $J^{(1)}$ might seem surprising in the light of the discussion on the second adiabatic invariant in subsection 2.2. When φ is non-zero, the average tangential and radial drifts (that now include the corresponding components of the $E \times B$ drift) are obtained by taking derivatives with respect to r and α keeping $\mathcal{E} = mv^2/2 + Ze\varphi/m$ and $\mu = v_\perp^2/(2B)$ constant. After this, one can perform the δ expansion and change to coordinates v and λ , obtaining (2.19) and (2.20). This process is explained step by step in Calvo *et al.* (2017).

note that $\partial_r J^{(0)}$ does not depend on α because B_0 is omnigenous. Sometimes, it will be useful to write $J^{(1)} = J_B^{(1)} + J_\varphi^{(1)}$, where

$$J_B^{(1)} = -\lambda v \int_{l_{b10}}^{l_{b20}} \frac{B_1}{\sqrt{1 - \lambda B_0}} dl \quad (2.23)$$

and

$$J_\varphi^{(1)} = -\frac{2Ze}{mv} \int_{l_{b10}}^{l_{b20}} \frac{\varphi^{(1)}}{\sqrt{1 - \lambda B_0}} dl. \quad (2.24)$$

Second, one has the quasineutrality equation. In the mass ratio expansion $\sqrt{m_e/m} \ll 1$, the non-adiabatic response of the electrons can be dropped, giving

$$\left(\frac{Z}{T} + \frac{1}{T_e}\right) \varphi^{(1)} = \frac{2\pi}{en} \int_0^\infty dv \int_{B_{0,\max}^{-1}}^{B_0^{-1}} d\lambda \frac{v^3 B_0}{|v_{||}^{(0)}|} g^{(1)}, \quad (2.25)$$

where $T_e(r)$ is the electron temperature. Note that the choice (2.17) implies that

$$\langle \varphi^{(1)} \rangle = 0, \quad (2.26)$$

where the flux-surface average is taken using B_0 . In addition, integration of (2.25) over trapped orbits, application of property (2.11) and of condition (2.17) implies

$$\int_0^{2\pi} J_\varphi^{(1)} d\alpha = 0. \quad (2.27)$$

Equations (2.18) and (2.25) are correct for values of the collisionality that include the neoclassical transport regimes known as $1/\nu$, $\sqrt{\nu}$ and superbanana-plateau regimes. In Calvo *et al.* (2017), it was explained why the equations stop to be valid at low enough values of the collisionality, so that they should be modified in case one is interested in describing, for example, the ν or superbanana regimes. In subsection 2.4, we explain how some of the quantities entering the neoclassical equations (2.18) and (2.25) behave when a large aspect ratio expansion is taken. In subsection 2.5, the perturbed omnigenous magnetic field that will be later used in the numerical examples is described.

2.4. Conventions and some useful scalings for large aspect ratio stellarators

Stellarators in operation today have large aspect ratio, $\epsilon^{-1} = R_0/a$. In Calvo *et al.* (2017), the scaling with $\epsilon \ll 1$ was not determined, and we would like to address this refinement in the present paper. In this subsection, some conventions that are convenient for $\epsilon \ll 1$ are explained, and the scaling with ϵ of several quantities entering (2.18) and (2.25) is provided for later use.

In a given flux surface, we write magnetic fields in large aspect ratio stellarators close to omnigenicity as

$$B = B_0 + \delta B_1, \quad (2.28)$$

where

$$B_0 = B_{00} + \tilde{B}_0, \quad (2.29)$$

B_{00} is constant and $\tilde{B}_0 \sim \epsilon B_{00}$. As for the non-omnigenous perturbation, we assume $B_1 \sim \epsilon B_{00}$. Note that if the aspect ratio is large, the meaningful measure of the size of the non-omnigenous perturbation is given by $\delta \sim |B - B_0|/|B_0 - B_{00}|$. This is why we have included a factor ϵ in our convention for the size of B_1 . The definition

$$\delta \sim \frac{B - B_0}{\epsilon B_0} \quad (2.30)$$

is valid both for large aspect ratio, $\epsilon \ll 1$, and tight aspect ratio, $\epsilon \sim 1$.

The radial derivative of B_0 at the surface of interest will also be needed. In our models, we will assume

$$\partial_r B_0 = \frac{\tilde{B}_0}{\epsilon R_0}. \quad (2.31)$$

We proceed to explain how different quantities appearing in the neoclassical equations scale with ϵ . We denote by Δ_{trapped} the size (measured in the coordinate λ) of the region of phase space corresponding to particles trapped in B_0 . Observing that the difference between the maximum and the minimum values of B_0 on the flux surface is $O(\epsilon B_{00})$, we infer that

$$\Delta_{\text{trapped}} \sim \epsilon B_{00}^{-1}. \quad (2.32)$$

Analogous reasons lead to conclude that the size of the parallel velocity for trapped particles is

$$v_{||}^{(0)} \sim \epsilon^{1/2} v_t. \quad (2.33)$$

The scaling of $\partial_r J^{(0)}$ depends on the size of the radial electric field, obtained by imposing ambipolarity of the neoclassical radial particle fluxes. For typical values $\varphi'_0 \sim \epsilon^{-1} T / (e R_0)$, the term containing the radial electric field dominates and

$$\partial_r J^{(0)} \sim \epsilon^{-3/2} v_t, \quad (2.34)$$

where we have assumed that the typical length of the omnigenous wells is R_0 . If the radial electric field is small, $|\varphi'_0| \lesssim T / (e R_0)$, then[†]

$$\partial_r J^{(0)} \sim \epsilon^{-1/2} v_t. \quad (2.35)$$

As for $J^{(1)}$, we have

$$J_B^{(1)} \approx -B_{00}^{-1} v \int_{l_{b10}}^{l_{b20}} \frac{B_1}{\sqrt{1 - \lambda B_0}} dl \sim \epsilon^{1/2} v_t R_0 \quad (2.36)$$

whereas

$$J_\varphi^{(1)} \sim \epsilon^{-1/2} v_t R_0 \frac{e \varphi^{(1)}}{T}. \quad (2.37)$$

Recall that $\varphi^{(1)}$ is one of the unknowns of the neoclassical equations and its size is to be determined.

The function Ψ appearing in (2.1) scales as

$$\Psi \sim \epsilon B_{00} R_0. \quad (2.38)$$

Regarding the plasma profile gradients, it is expected that, generically,

$$\Upsilon \sim \frac{1}{\epsilon R_0}. \quad (2.39)$$

In large aspect ratio stellarators, the collision term on the right-hand side of (2.18) is dominated by the pitch-angle scattering piece of the collision operator,

$$C_{ii}^{\ell(0)}[g^{(1)}] \approx \nu_\lambda \frac{v_{||}^{(0)}}{v^2 B_{00}^2} \partial_\lambda \left(v_{||}^{(0)} \partial_\lambda g^{(1)} \right), \quad (2.40)$$

[†] See, for example, Klinger *et al.* (2017), where radial electric field profiles are shown such that $\varphi'_0 = 0$ at some radial position.

where

$$\nu_\lambda(v) = \frac{3\sqrt{\pi}}{2\tau_{ii}} \frac{\operatorname{erf}\left(v\sqrt{m/(2T)}\right) - \chi\left(v\sqrt{m/(2T)}\right)}{\left(v\sqrt{m/(2T)}\right)^3} \quad (2.41)$$

is the ion-ion collision frequency,

$$\tau_{ii} = 6\sqrt{2}\pi^{3/2}\varepsilon_0^2 m^{1/2} T^{3/2} / (Z^4 e^4 n \ln \Lambda), \quad (2.42)$$

$\ln \Lambda$ is the Coulomb logarithm, ε_0 is the vacuum permittivity,

$$\operatorname{erf}(x) = \frac{2}{\sqrt{\pi}} \int_0^x e^{-y^2} dy \quad (2.43)$$

and

$$\chi(x) = \frac{\operatorname{erf}(x) - (2x/\sqrt{\pi}) \exp(-x^2)}{2x^2}. \quad (2.44)$$

Employing the estimates above for the scaling of Δ_{trapped} and $v_{||}^{(0)}$ with ϵ , we find

$$C_{ii}^{\ell(0)}[g^{(1)}] \sim \frac{\nu_*}{\epsilon} \frac{v_t}{R_0} g^{(1)}, \quad (2.45)$$

which is the typical size of the collision term across the trapped region. It is important to realize that the condition for low collisionality ions, that reads $\nu_* \ll 1$ for $\epsilon \sim 1$, becomes[†] $\nu_* \ll \epsilon^{3/2}$ for $\epsilon \ll 1$. This result is derived by comparing the factor in front of $g^{(1)}$ on the right-hand side of (2.45) with the typical frequency of the parallel particle motion, which is $O(\epsilon^{1/2} v_t / R_0)$ when $\epsilon \ll 1$.

Finally, we point out that (see (2.40)), when $\epsilon \ll 1$, we can define

$$\nu_* := \frac{\nu_\lambda(v_t) R_0}{v_t} \quad (2.46)$$

as the expression for the collisionality and

$$\rho_* := \frac{\sqrt{mT}}{ZeB_{00}R_0} \quad (2.47)$$

for the normalized Larmor radius.

2.5. Model magnetic field close to omnigenicity

In order to define a specific omnigenous field B_0 for the numerical examples provided in subsequent sections, we follow Cary & Shasharina (1997) and Landreman & Catto (2012). The description is easier in Boozer coordinates (Boozer 1981). We denote by θ and ζ the poloidal and toroidal Boozer angles, respectively. We use the construction explained in section V of Landreman & Catto (2012) with $M = 1$ and $N = 4$ (which means that the contours of B_0 close on themselves after 4 poloidal turns and 1 toroidal turn) and with rotational transform $t = 1.05$. We take[‡]

$$\tilde{B}_0(\theta, \zeta) = \epsilon B_{00} \cos \eta(\theta, \zeta), \quad (2.48)$$

where the function η is obtained as in equation (73) of Landreman & Catto (2012). In figure 2 we show a plot of an omnigenous magnetic field of the form just introduced.

[†] We point out that the range $\epsilon^{3/2} \ll \nu_* \ll 1$ corresponds to the plateau regime.

[‡] In order to avoid any confusion, we point out that the meaning of the symbol ϵ in our paper and in Landreman & Catto (2012) is not exactly the same. What we call ϵ would be

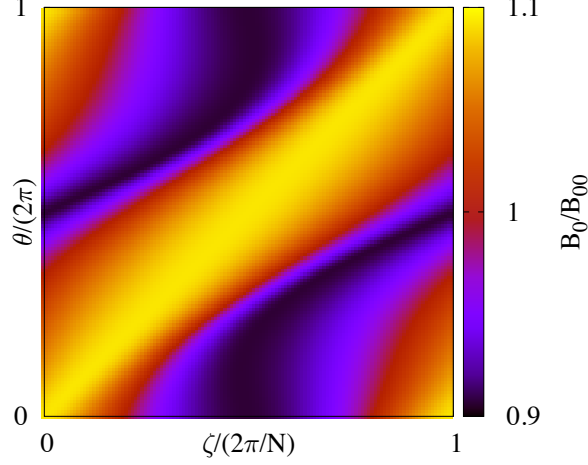


FIGURE 2. Plot of B_0 for the model omnigenous magnetic field described at the beginning of subsection 2.5; that is, $B_0 = B_{00} + \tilde{B}_0$, with \tilde{B}_0 of the form (2.48). Here, $\epsilon = 0.1$.

As for the non-omnigenous perturbation, we take

$$B_1 = \epsilon B_{00} \cos(2\theta). \quad (2.49)$$

Note that $B = B_0 + \delta B_1$ is symmetric under the transformation $(\theta, \zeta) \mapsto (-\theta, -\zeta)$. Magnetic fields with this property are called *stellarator symmetric* (Dewar & Hudson 1998). Stellarator designs typically impose this symmetry on the magnetic configuration, and from here on we always assume that our magnetic field satisfies it.

Given Boozer angles $\{\theta, \zeta\}$, there are many different ways to define coordinates $\{\alpha, l\}$. First, one has to choose a closed curve \mathcal{C} that is not contractible to a point. A simple choice is to take the curve $\zeta = 0$. Then,

$$\alpha := \theta - \epsilon \zeta. \quad (2.50)$$

As for the arc length l ,

$$l(\alpha, \zeta) = \int_0^\zeta \frac{1}{\hat{\mathbf{b}} \cdot \nabla_{\zeta'}} d\zeta', \quad (2.51)$$

where the integral on the right-hand side is taken at constant α and l_{\max} is determined by the intersection of the field line with \mathcal{C} when it goes all the way around the torus.

3. Dependence of $\varphi^{(1)}$ on the collisionality and the radial electric field: a realistic numerical example

Let us take realistic, stellarator reactor relevant parameters, $\rho_* = 1.87 \times 10^{-4}$ and $\epsilon = 0.1$, and let us employ the model magnetic field close to omnigenicity $B = B_0 + \delta B_1$ described in subsection 2.5 (see (2.29), (2.48) and (2.49)). As for the profiles, we take $n'/n = -(\epsilon R_0)^{-1}$ and $T' = 0$. We solve (2.18) and (2.25) with the code KNOSOS, and in figure 3 we represent the size of $\varphi^{(1)}$ versus ν_* . We plot curves corresponding to $\varphi'_0 = 0$

called $\epsilon/(1 + \epsilon)$ in Landreman & Catto (2012). What we call $B_{00}(1 - \epsilon)$ would be called \tilde{B} in Landreman & Catto (2012).

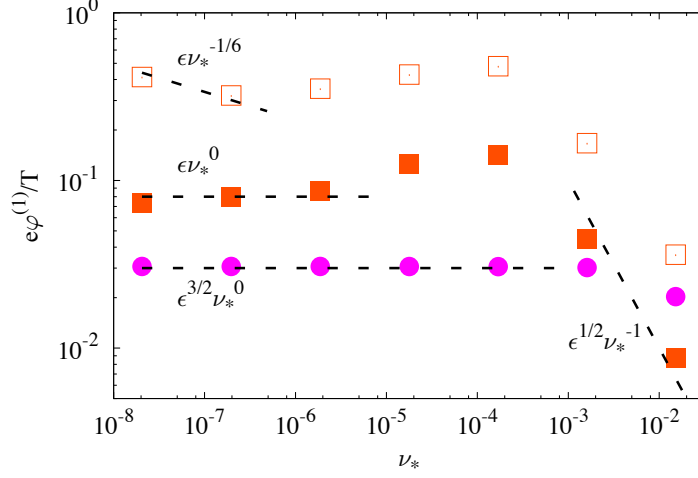


FIGURE 3. Size of $\varphi^{(1)}$ as a function of the collisionality for a plasma with $\rho_* = 1.87 \times 10^{-4}$ and magnetic configuration defined at the end of subsection 2.5 with $\epsilon = 0.1$. The circles correspond to results with $\varphi'_0 = 2\epsilon^{-1}T/(eR_0)$. The squares correspond to $\varphi'_0 = 0$. Empty squares give the size of $\varphi^{(1)}$. Full squares give the size of $\varphi^{(1)}$ at generic points (see the main text for the explanation on the difference between size of $\varphi^{(1)}$ and size of $\varphi^{(1)}$ at generic points). The important difference between the curves consisting of empty and full squares is that, for $\nu_* \ll \rho_*$, the first one behaves as $\nu_*^{-1/6}$ and the second one does not vary with ν_* .

and to $\varphi'_0 = 2\epsilon^{-1}T/(eR_0)$. In this plot and in subsequent ones representing $\varphi^{(1)}$ versus ν_* , we typically take the maximum value of $\varphi^{(1)}$ on the flux surface, and this is what we generally understand by “the size of $\varphi^{(1)}$ ”. However, there are regimes (see subsection 4.3) in which the scaling of $\varphi^{(1)}$ at special points (lying in a very small spatial region associated with certain resonant trajectories) is different from that of $\varphi^{(1)}$ at generic points, far from the special points. When such regimes exist, we usually plot two curves and distinguish between “the size of $\varphi^{(1)}$ ” (see, for example, empty squares in figure 3), given by the maximum of $\varphi^{(1)}$ on the flux surface, and “the size of $\varphi^{(1)}$ at generic points” (see, for example, full squares in figure 3). In order to compute the size of $\varphi^{(1)}$ at generic points, we take a spatial average of $\varphi^{(1)}$ in a region where $\varphi^{(1)}$ is positive and which is far from the special points.

The dependence of $\varphi^{(1)}$ on the collisionality and on the radial electric field shown in figure 3 is non-trivial. Understanding the different regimes encoded in a plot like figure 3 is the main subject of this paper. We will identify and study these regimes in Section 4. As we will explain below, in order to have very clear numerical scalings in all the asymptotic regimes that (2.18) and (2.25) admit, in Section 4 we will employ extremely small values of ρ_* and ϵ in our numerical checks. The reader that prefers to skip the mathematical derivations of Section 4 can go directly to table 1 in Section 5 for a collection of the main analytical results.

4. Asymptotic regimes of $\varphi^{(1)}$ at low collisionality

In this section, we discuss the solution $\varphi^{(1)}$ determined by equations (2.18) and (2.25) in three asymptotic low collisionality regimes. Namely, the $1/\nu$ regime, the $\sqrt{\nu}$ regime and the superbanana-plateau regime (the names of the regimes are due to the scaling of the radial neoclassical fluxes with collisionality, not necessarily to the scaling of $\varphi^{(1)}$, as we will explain below). The subsection devoted to each regime will start with a discussion valid for arbitrary aspect ratio. Then, the results will be particularized for large aspect ratio stellarators and numerical examples of the most relevant analytical results will follow. In the course of the analytical derivations, it will become clear that in order to clearly distinguish all the asymptotic regimes that equations (2.18) and (2.25) admit, the quantities ρ_* , $\rho_*/\epsilon^{1/2}$ and ρ_*/ϵ need to be sufficiently separated from each other. This is why, in what follows, we will take artificially small values for ρ_* and ϵ , so that there is enough room between those quantities in our numerical examples. In these examples, we will always take $\rho_* = 1.1 \times 10^{-12}$, $n'/n = -(\epsilon R_0)^{-1}$ and $T' = 0$, and we will always employ the model magnetic field close to omnigenity defined in subsection 2.5 (recall equations (2.29), (2.48) and (2.49)). We will use different values of ϵ and φ'_0 that will be specified where appropriate.

4.1. The $1/\nu$ regime

For tight aspect ratio stellarators, the $1/\nu$ regime corresponds to $\rho_* \ll \nu_* \ll 1$. In this situation, the first term on the left-hand side of (2.18) is negligible compared to the term on the right-hand side,

$$\left| \partial_r J^{(0)} \partial_\alpha g^{(1)} \right| \ll \left| \sum_\sigma \frac{Ze\Psi}{m} \int_{l_{b10}}^{l_{b20}} \frac{dl}{|v_{||}^{(0)}|} C_{ii}^{\ell(0)} \left[g^{(1)} \right] \right|. \quad (4.1)$$

The correction to the Maxwellian distribution in the $1/\nu$ regime is therefore found by integrating the expression

$$\sum_\sigma \frac{Ze\Psi}{m} \int_{l_{b10}}^{l_{b20}} |v_{||}^{(0)}|^{-1} C_{ii}^{\ell(0)} \left[g_{1/\nu}^{(1)} \right] dl = \partial_\alpha J^{(1)} \Upsilon_{FM}. \quad (4.2)$$

Below, we will find useful to distinguish between $g_{1/\nu}^{(1)}[J_B^{(1)}]$ and $g_{1/\nu}^{(1)}[J_\varphi^{(1)}]$, where

$$\sum_\sigma \frac{Ze\Psi}{m} \int_{l_{b10}}^{l_{b20}} |v_{||}^{(0)}|^{-1} C_{ii}^{\ell(0)} \left[g_{1/\nu}^{(1)}[J_B^{(1)}] \right] dl = \partial_\alpha J_B^{(1)} \Upsilon_{FM} \quad (4.3)$$

and

$$\sum_\sigma \frac{Ze\Psi}{m} \int_{l_{b10}}^{l_{b20}} |v_{||}^{(0)}|^{-1} C_{ii}^{\ell(0)} \left[g_{1/\nu}^{(1)}[J_\varphi^{(1)}] \right] dl = \partial_\alpha J_\varphi^{(1)} \Upsilon_{FM}, \quad (4.4)$$

and therefore $g_{1/\nu}^{(1)} = g_{1/\nu}^{(1)}[J_B^{(1)}] + g_{1/\nu}^{(1)}[J_\varphi^{(1)}]$. We note that

$$g_{1/\nu}^{(1)}[J_B^{(1)}] \sim \frac{\rho_*}{\nu_*} \frac{n}{v_t^3} \quad (4.5)$$

and

$$g_{1/\nu}^{(1)}[J_\varphi^{(1)}] \sim \frac{\rho_*}{\nu_*} \frac{e\varphi^{(1)}}{T} \frac{n}{v_t^3}. \quad (4.6)$$

The equation for $\varphi^{(1)}$ reads (recall (2.25))

$$\varphi^{(1)} = \left(\frac{Z}{T} + \frac{1}{T_e} \right)^{-1} \frac{2\pi B_0}{en} \int_0^\infty dv v^3 \int_{B_{0,\max}^{-1}}^{B_0^{-1}} d\lambda |v_{||}^{(0)}|^{-1} \left(g_{1/\nu}^{(1)}[J_\varphi^{(1)}] + g_{1/\nu}^{(1)}[J_B^{(1)}] \right). \quad (4.7)$$

Using (4.6) and $\rho_* \ll \nu_*$, and comparing the size of the left-hand side of (4.7) with the size of the term on the right-hand side containing $g_{1/\nu}^{(1)}[J_\varphi^{(1)}]$, we conclude that the latter can be dropped. Hence, $\varphi^{(1)}$ is calculated as

$$\varphi^{(1)} = \left(\frac{Z}{T} + \frac{1}{T_e} \right)^{-1} \frac{2\pi B_0}{en} \int_0^\infty dv v^3 \int_{B_{0,\max}^{-1}}^{B_0^{-1}} d\lambda |v_{||}^{(0)}|^{-1} g_{1/\nu}^{(1)}[J_B^{(1)}]. \quad (4.8)$$

Then, in the $1/\nu$ regime (see (4.5) and (4.6)),

$$g^{(1)} \sim \frac{\rho_*}{\nu_*} \frac{n}{v_t^3} \quad (4.9)$$

and

$$\varphi^{(1)} \sim \frac{\rho_*}{\nu_*} \frac{T}{e}. \quad (4.10)$$

If B_0 and B_1 are stellarator symmetric, $J_B^{(1)}$ is symmetric and, consequently, $\partial_\alpha J_B^{(1)}$ is antisymmetric. Since the collision operator does not change the symmetry, the solution $g_{1/\nu}^{(1)}$ of (4.2) is antisymmetric. Finally, $\varphi^{(1)}$, obtained from (4.8), is stellarator antisymmetric.

4.1.1. The $1/\nu$ regime in a large aspect ratio stellarator

As indicated by the end of subsection 2.4, when ϵ is small the low collisionality condition reads $\nu_* \ll \epsilon^{3/2}$. How small ν_* can be before the tangential drifts start to count depends on their size, as will be discussed mainly in subsections 4.2.1 and 4.2.2.

Let us refine the estimates (4.9) and (4.10) for the distribution function and the electrostatic potential when $\epsilon \ll 1$. The drift-kinetic equation for $\epsilon \ll 1$ is

$$\frac{2Ze\Psi}{mB_{00}^2} \partial_\lambda \left[\left(\int_{l_{b10}}^{l_{b20}} \sqrt{1 - \lambda B_0} dl \right) \partial_\lambda g_{1/\nu}^{(1)} \right] = \frac{v}{\nu_\lambda} \partial_\alpha J^{(1)} \Upsilon F_M. \quad (4.11)$$

Employing the scalings of subsection 2.4, it is easy to infer that

$$g_{1/\nu}^{(1)}[J_B^{(1)}] \sim \frac{\rho_*}{\nu_*} \frac{n}{v_t^3} \quad (4.12)$$

and

$$g_{1/\nu}^{(1)}[J_\varphi^{(1)}] \sim \epsilon^{-1/2} \frac{\rho_*}{\nu_*} \frac{J_\varphi^{(1)}}{v_t R_0} \frac{n}{v_t^3}. \quad (4.13)$$

Next, we apply the $\epsilon \ll 1$ expansion to (4.7). We must treat two cases separately. If

$$\epsilon^{-1/2} \rho_* \ll \nu_* \ll \epsilon^{3/2}, \quad (4.14)$$

then the first term on the right side of (4.7) is negligible with respect to the left-hand side. Using that $\Delta_{\text{trapped}} \sim \epsilon B_{00}^{-1}$, we find

$$\varphi^{(1)} \sim \epsilon^{1/2} \frac{\rho_*}{\nu_*} \frac{T}{e}. \quad (4.15)$$

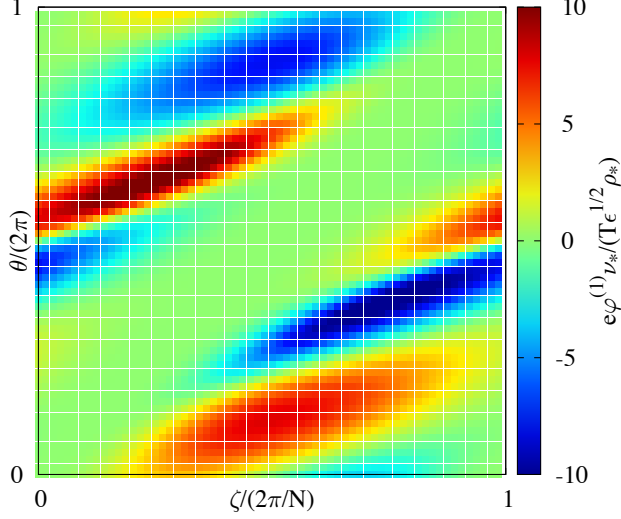


FIGURE 4. Contour plot of $\varphi^{(1)}$ for $\epsilon = 1.1 \times 10^{-4}$, $\nu_* = 10^{-7}$ and $\varphi'_0 = 0$.

And noting that $g_{1/\nu}^{(1)}[J_\varphi^{(1)}] \ll g_{1/\nu}^{(1)}[J_B^{(1)}]$,

$$g^{(1)} \sim \frac{\rho_*}{\nu_*} \frac{n}{v_t^3}. \quad (4.16)$$

Then, both $\varphi^{(1)}$ and $g^{(1)}$ scale as ν_*^{-1} . The fact that $\varphi^{(1)}$ is antisymmetric is also clear. In figure 4, a contour plot of $\varphi^{(1)}$ on the magnetic surface is provided for a set of values such that (4.14) holds.

However, if $\nu_* \sim \epsilon^{-1/2}\rho_*$ or smaller, the first term on the right-hand side of (4.7) can become comparable to the left-hand side. Let us study the asymptotic regime

$$\nu_* \ll \epsilon^{-1/2}\rho_*. \quad (4.17)$$

From (4.7) we learn that $\varphi^{(1)}$ depends on l only through B_0 . This will be important in a moment. When (4.17) holds, the left-hand side of (4.7) is small compared to the term on the right-hand side that involves $\varphi^{(1)}$. Then, we can write

$$\int_0^\infty dv v^2 \int_{B_{0,\max}^{-1}}^{B_0^{-1}} d\lambda \frac{1}{\sqrt{1-\lambda B_0}} g_{1/\nu}^{(1)} = 0, \quad (4.18)$$

where $g_{1/\nu}^{(1)}$ is the solution of (4.11). For the argument that follows, we find it convenient to write $J^{(1)}$ as

$$J^{(1)} = - \int_{B_{0,\min}}^{B_0} \frac{G}{\sqrt{1-\lambda \hat{B}}} d\hat{B}. \quad (4.19)$$

Here, $B_{0,\min}$ is the minimum of B_0 ,

$$G(r, \alpha, \hat{B}, \beta, v) := \sum_{\beta=-1}^1 \left(\frac{B_1 v}{B_{00}} + \frac{2Ze\varphi^{(1)}}{mv} \right) \frac{1}{|\partial_t B_0|} \quad (4.20)$$

and we have used the magnitude of B_0 as the integration variable in (4.19). Since there are two values[†] of l corresponding to each value $B_0 = \hat{B}$, we introduce the discrete coordinate $\beta = \pm 1$. The value $\beta = -1$ labels the branch of the magnetic well where $\partial_l B_0 < 0$ and the value $\beta = 1$ labels the branch where $\partial_l B_0 \geq 0$. On the right-hand side of (4.20), every function is understood to be expressed using \hat{B} and β instead of l . In particular, we note that, in general, $|\partial_l B_0|(\hat{B}, \beta) \neq |\partial_l B_0|(\hat{B}, -\beta)$.

It is clear that

$$\int_0^\infty v^2 g_{1/\nu}^{(1)} dv = 0 \quad (4.21)$$

gives the solution of (4.18) and that, by imposing (4.21), we obtain a relation between the orbit integrals of B_1 and $\varphi^{(1)}$. The orbit integral of a function can be interpreted as a transformation that replaces the coordinate l by the coordinate λ . This can be viewed as an Abel transform, and an explicit inversion formula is given in Appendix A. In principle, the inversion cannot distinguish between two points of the magnetic well with the same value of B_0 (this is quite intuitive when we use the magnitude of B_0 as the integration variable, as we have done in (4.19)). Carrying out the integral in v on the left-hand side of (4.21), we arrive at

$$\sum_{\beta=-1}^1 \frac{Ze\varphi^{(1)}}{T} \frac{1}{|\partial_l B_0|} = -2.83 \frac{n'/n + Ze\varphi'_0/T + 2.33T'/T}{n'/n + Ze\varphi'_0/T + 1.33T'/T} \sum_{\beta=-1}^1 \frac{B_1}{B_{00}} \frac{1}{|\partial_l B_0|}. \quad (4.22)$$

Recalling that $\varphi^{(1)}$ depends on l only through B_0 (see equation (4.7)), we finally obtain the explicit solution

$$\frac{Ze\varphi^{(1)}}{T} = -2.83 \frac{n'/n + Ze\varphi'_0/T + 2.33T'/T}{n'/n + Ze\varphi'_0/T + 1.33T'/T} \frac{\sum_{\beta=-1}^1 (B_1/B_{00}) |\partial_l B_0|^{-1}}{\sum_{\beta=-1}^1 |\partial_l B_0|^{-1}}. \quad (4.23)$$

From (4.23) we infer that in this regime $\varphi^{(1)}$ is stellarator symmetric and that its size, in general, is

$$\varphi^{(1)} \sim \epsilon \frac{T}{e}. \quad (4.24)$$

We note that for particular combinations of the profile gradients, $\varphi^{(1)}$ can get larger because the denominator of (4.23) can become small. This will be studied elsewhere.

In figure 5, a contour plot of $\varphi^{(1)}$ on the magnetic surface is provided for a set of values that satisfy (4.17).

Finally, we have (see (4.12) and (4.13))

$$g_{1/\nu}^{(1)} \sim g_{1/\nu}^{(1)}[J_\varphi^{(1)}] \sim g_{1/\nu}^{(1)}[J_B^{(1)}] \sim \frac{\rho_*}{\nu_*} \frac{n}{v_t^3}. \quad (4.25)$$

In figure 6, and for $\varphi'_0 = 0$, we illustrate the scaling of $\varphi^{(1)}$ and of

$$n_B := \int g_{1/\nu}^{(1)}[J_B^{(1)}] d^3v \sim \frac{\rho_*}{\nu_*} n \quad (4.26)$$

in a range of collisionality values such that both regimes, (4.14) and (4.17), are observed.

[†] For simplicity in the presentation, we assume that the omnigenous wells are such that exactly two points in the well take each value $B_0 = \hat{B}$ (except for the value $B_{0,\min}$, which is reached at a single point). There exist omnigenous magnetic fields with more complicated wells (Parra *et al.* 2015), and in those cases the discrete coordinate β would need to label more than two branches.

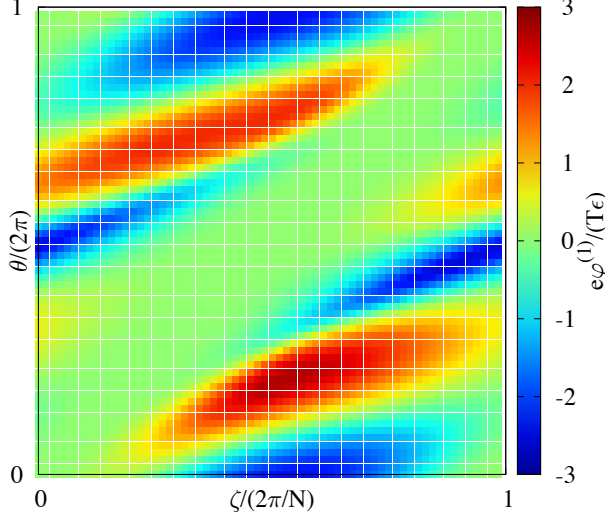


FIGURE 5. Contour plot of $\varphi^{(1)}$ for $\epsilon = 1.1 \times 10^{-4}$, $\nu_* = 5.8 \times 10^{-11}$ and $\varphi'_0 = 0$.

Whereas $\varphi^{(1)}$ and n_B have the same scaling with ν_* in the regime (4.14), they scale differently in the regime (4.17).

4.2. The $\sqrt{\nu}$ regime

We turn to discuss collisionality regimes with $\nu_* \ll \rho_* \ll 1$. In this situation, as explained at length in Calvo *et al.* (2017), the behavior of both the radial neoclassical fluxes and $\varphi^{(1)}$ depends on the zeroes of $\partial_r J^{(0)}$.

When $\nu_* \ll \rho_*$, the collision term in (2.18) is negligible compared to the first term on the left-hand side,

$$\left| \sum_{\sigma} \frac{Ze\Psi}{m} \int_{l_{b10}}^{l_{b20}} \frac{dl}{|v_{||}^{(0)}|} C_{ii}^{\ell(0)}[g^{(1)}] \right| \ll \left| \partial_r J^{(0)} \partial_{\alpha} g^{(1)} \right|. \quad (4.27)$$

Hence, to lowest order in an expansion in ν_*/ρ_* ,

$$g^{(1)} = g_0 + \dots, \quad (4.28)$$

where g_0 is the solution of

$$-\partial_r J^{(0)} \partial_{\alpha} g_0 + \partial_{\alpha} J^{(1)} \Upsilon F_M = 0. \quad (4.29)$$

This equation can be readily solved, obtaining an explicit expression for g_0 ,

$$g_0 = \frac{1}{\partial_r J^{(0)}} \left(J^{(1)} - \frac{1}{2\pi} \int_0^{2\pi} J^{(1)} d\alpha \right) \Upsilon F_M, \quad (4.30)$$

where we have chosen $\int_0^{2\pi} g_0 d\alpha = 0$ to fix the integration constant. From (4.30), it is clear that the solution g_0 is not valid at phase space points where $\partial_r J^{(0)}$ vanishes, and we devote subsection 4.3 to those points. However, if $\partial_r J^{(0)}$ does not vanish at any point of phase space (or if it vanishes only for values of the velocity $v \gg v_t$, that are irrelevant

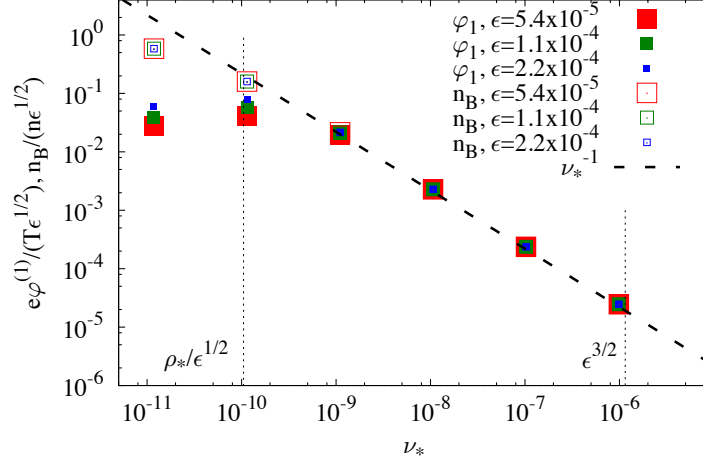


FIGURE 6. Scaling of $\varphi^{(1)}$ and n_B (evaluated at the point of the flux surface where they reach their maximum values) with ν_* and ϵ . Here, $\varphi'_0 = 0$. The regimes (4.14) and (4.17) are confirmed numerically. The central value $\epsilon = 1.1 \times 10^{-4}$ has been used to draw the thin dotted lines indicating where the collisionality values $\rho_*/\epsilon^{1/2}$ and $\epsilon^{3/2}$ are located.

because their effect is suppressed by the smallness of the Maxwellian distribution), (4.30) is enough to correctly determine $\varphi^{(1)}$ via the quasineutrality equation

$$\varphi^{(1)} = \left(\frac{Z}{T} + \frac{1}{T_e} \right)^{-1} \frac{2\pi B_0}{en} \int_0^\infty dv v^3 \int_{B_0^{-1}}^{B_0^{-1}} d\lambda |v_{||}^{(0)}|^{-1} g_0. \quad (4.31)$$

In this case, $\varphi^{(1)}$ is stellarator symmetric (due to the fact that the expression (4.30) for g_0 does not involve derivatives of B along the flux surface) and does not scale with collisionality,

$$\varphi^{(1)} \sim \frac{T}{e}. \quad (4.32)$$

As proven in Calvo *et al.* (2017), g_0 does not contribute to the radial neoclassical fluxes. They are determined by corrections to g_0 in (4.28) that are localized in a region of phase space that has a typical size $\Delta_{\sqrt{\nu}} \sim \sqrt{\nu_*/\rho_*}$ in the coordinate λ . This small layer produces the scaling with collisionality that justifies the name of this regime, the $\sqrt{\nu}$ regime.

If the aspect ratio is large, it is interesting to distinguish two cases (mostly in connection to the solutions of the quasineutrality equation), to which we devote subsections 4.2.1 and 4.2.2.

4.2.1. Large aspect ratio and large tangential drift, $\partial_r J^{(0)} \sim \epsilon^{-3/2} v_t R_0$

If $\partial_r J^{(0)} \sim \epsilon^{-3/2} v_t R_0$, the inequality (4.27) holds provided that $\nu_* \ll \epsilon^{-1} \rho_*$. Hence, the $1/\nu$ regime takes place in the range

$$\epsilon^{-1} \rho_* \ll \nu_* \ll \epsilon^{3/2}. \quad (4.33)$$

In particular, the regime defined by (4.17) is not observed because the tangential drift starts to count for collisionalities much larger than $\epsilon^{-1/2}\rho_*$. It can be observed, however, when the tangential drift is smaller (see subsection 4.2.2).

As pointed out in subsection 2.4, $\partial_r J^{(0)} \sim \epsilon^{-3/2}v_t R_0$ corresponds to $\varphi'_0 \sim \epsilon^{-1}T/(eR_0)$, which is the standard size of the radial electric field in a large aspect ratio stellarator. The derivation of the radial fluxes in this regime can be found, for example, in Galeev & Sagdeev (1979); Ho & Kulsrud (1987).

Let us start the discussion about $\varphi^{(1)}$ by writing (4.31) more explicitly. Inserting in (4.31) the expression for g_0 (see (4.30)) and rearranging a bit, we get

$$\begin{aligned} \varphi^{(1)} - \frac{2\pi}{en} \left(\frac{Z}{T} + \frac{1}{T_e} \right)^{-1} \int_0^\infty dv \int_{B_{0,\max}^{-1}}^{B_0^{-1}} d\lambda \frac{v^3 B_0}{|v_{||}^{(0)}|} \frac{\Upsilon F_M}{\partial_r J^{(0)}} \tilde{J}_\varphi^{(1)} \\ = \frac{2\pi}{en} \left(\frac{Z}{T} + \frac{1}{T_e} \right)^{-1} \int_0^\infty dv \int_{B_{0,\max}^{-1}}^{B_0^{-1}} d\lambda \frac{v^3 B_0}{|v_{||}^{(0)}|} \frac{\Upsilon F_M}{\partial_r J^{(0)}} \tilde{J}_B^{(1)}, \end{aligned} \quad (4.34)$$

where

$$\tilde{J}_B^{(1)} = J_B^{(1)} - \frac{1}{2\pi} \int_0^{2\pi} J_B^{(1)} d\alpha \quad (4.35)$$

and

$$\tilde{J}_\varphi^{(1)} = J_\varphi^{(1)} - \frac{1}{2\pi} \int_0^{2\pi} J_\varphi^{(1)} d\alpha. \quad (4.36)$$

In (4.36) we have emphasized that only the component of $J_\varphi^{(1)}$ that fluctuates in α enters (4.34) although, strictly speaking, it is superfluous due to (2.27).

Recalling the estimates in subsection 2.4, it is straightforward to see that the second term on the left-hand side of (4.34) is smaller than the first one by a factor $\epsilon^{1/2}$. Hence, the size of $\varphi^{(1)}$ is determined by the size of the right-hand side of (4.34). That is,

$$\varphi^{(1)} \sim \epsilon^{3/2} \frac{T}{e}. \quad (4.37)$$

This scaling is consistent with (4.15) when $\nu_* \sim \epsilon^{-1}\rho_*$. In figure 7, a contour plot of $\varphi^{(1)}$ corresponding to $\partial_r J^{(0)} \sim \epsilon^{-3/2}v_t R_0$ and $\nu_* \ll \epsilon^{-1}\rho_*$ is shown. In figure 8, the collisionality-independent scaling (4.37) for $\varphi^{(1)}$ is numerically checked.

4.2.2. Large aspect ratio and small tangential drift, $\partial_r J^{(0)} \sim \epsilon^{-1/2}v_t R_0$

If $\partial_r J^{(0)} \sim \epsilon^{-1/2}v_t R_0$, (4.27) is satisfied when $\nu_* \ll \rho_*$. Therefore, for such typical size of the tangential drifts, the $1/\nu$ regime happens for collisionality values

$$\rho_* \ll \nu_* \ll \epsilon^{3/2}. \quad (4.38)$$

To be precise, in the range $\rho_* \ll \nu_* \ll \epsilon^{-1/2}\rho_*$, the subregime (4.17) of the $1/\nu$ regime will be observed.

When $\partial_r J^{(0)} \sim \epsilon^{-1/2}v_t R_0$, the left-hand side of (4.31) can be neglected compared to the term on the right-hand side containing $\varphi^{(1)}$, so that we have

$$\int_0^\infty dv v^2 \int_{B_{0,\max}^{-1}}^{B_0^{-1}} d\lambda \frac{g_0}{\sqrt{1 - \lambda B_0}} = 0, \quad (4.39)$$

which can be solved by finding the solution of

$$\int_0^\infty dv v^2 g_0 = 0. \quad (4.40)$$

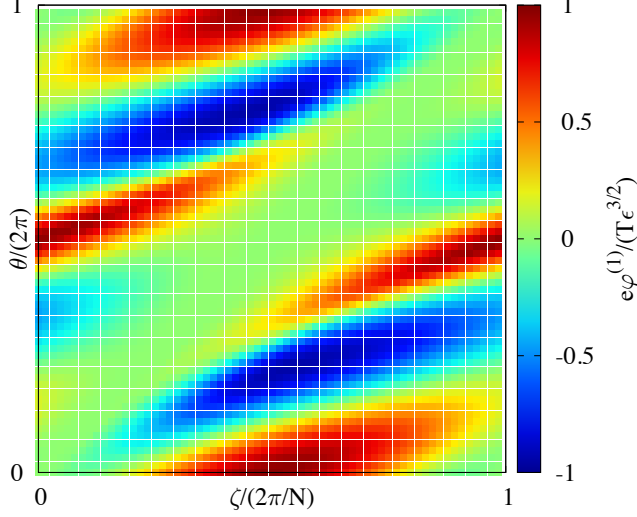


FIGURE 7. Contour plot of $\varphi^{(1)}$ for $\epsilon = 1.1 \times 10^{-4}$, $\nu_* = 1.1 \times 10^{-10}$ and $\varphi'_0 = 2\epsilon^{-1}T/(eR_0)$.

One could formally proceed as done after equation (4.17), but it seems difficult to find a completely explicit solution for $\varphi^{(1)}$ due to the relatively complicated dependence of $\partial_r J^{(0)}$ on v and λ . In any case, it is clear that imposing (4.40) implies

$$J_\varphi^{(1)} \sim \epsilon^{1/2} v_t R_0 \quad (4.41)$$

and, therefore,

$$\varphi^{(1)} \sim \epsilon \frac{T}{e}. \quad (4.42)$$

In addition, from (4.40) we can infer that $\varphi^{(1)}$ is stellarator symmetric.

Note that for $\nu_* \sim \rho_*$, expression (4.42) matches (4.24).

4.3. Superbanana-plateau regime

In this subsection, we treat cases with $\nu_* \ll \rho_* \ll 1$ and such that $\partial_r J^{(0)}$ vanishes for $v \lesssim v_t$. Subsections 4.1 and 4.2, although brief, were self-contained to a large extent. In this subsection we will refer the reader to Calvo *et al.* (2017) more frequently for the derivation of particularly technical results.

The zeroes of $\partial_r J^{(0)}$ correspond to ‘resonant’ points of phase space where the orbit-averaged tangential component of the magnetic and $E \times B$ drifts cancel each other.

Recall equation (2.19). The condition $\partial_r J^{(0)} = 0$ can be compactly expressed as

$$\lambda \overline{\partial_r B_0}(r, \lambda) = -\frac{2Ze\varphi'_0(r)}{mv^2}, \quad (4.43)$$

where

$$\overline{(\cdot)} = \frac{1}{\tau_b^{(0)}} \sum_\sigma \int_{l_{b10}}^{l_{b20}} (\cdot) |v_{||}^{(0)}|^{-1} dl \quad (4.44)$$

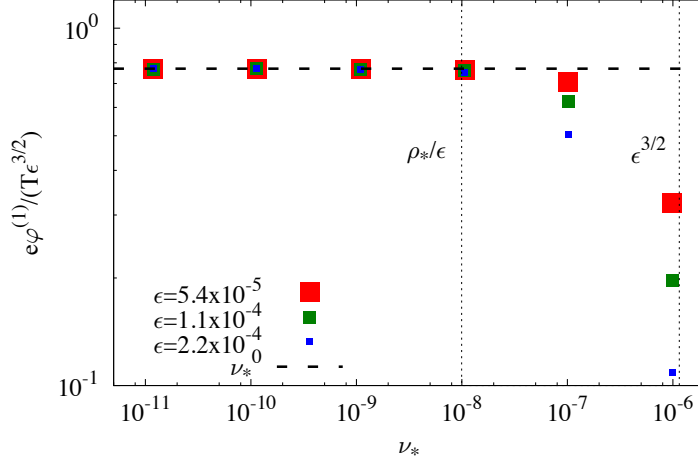


FIGURE 8. Scaling of $\varphi^{(1)}$ with ν_* and ϵ (evaluated at the point of the flux surface where it reaches its maximum value) in a range of values of the collisionality where (4.37) is observed. Here, $\varphi'_0 = 2\epsilon^{-1}T/(eR_0)$.

denotes orbit average and

$$\tau_b^{(0)}(r, v, \lambda) = 2 \int_{l_{b10}}^{l_{b20}} |v_{||}^{(0)}|^{-1} dl \quad (4.45)$$

is the time that it takes for the particle to complete the orbit in the magnetic field B_0 . A necessary (but not sufficient) condition for this equation to have solutions for $v \lesssim v_t$ is

$$\frac{Ze|\varphi'_0|}{T} \lesssim \frac{1}{R_0}. \quad (4.46)$$

That is, the effect of the resonances is expected to be important for relatively small values of the radial electric field. When $\nu_* \ll \rho_* \ll 1$ and $Ze|\varphi'_0|/T \gg R_0^{-1}$, the treatment of subsection (4.2) applies.

From here on, let us assume $\nu_* \ll \rho_* \ll 1$ and condition (4.46) in the rest of this subsection, and let us also assume that, for $v \lesssim v_t$, there exists one solution in λ of the resonance condition (4.43), that we denote by $\lambda_r(r, v, \varphi'_0)$. In general, λ_r will be defined only for some values of r , v and φ'_0 . For fixed r and φ'_0 , we denote by I the interval in v for which λ_r is defined.

We can expand the drift-kinetic equation (2.18) around the position of the resonance. Defining $\xi = \lambda - \lambda_r(r, v, \varphi'_0)$ and writing the drift-kinetic equation in coordinates v and ξ , we have

$$\partial_\lambda \partial_r J_r^{(0)} \xi \partial_\alpha g_{rl} + k \partial_\xi^2 g_{rl} = \left(\partial_\alpha J_{B,r}^{(1)} + \partial_\alpha \widehat{J_\varphi^{(1)}} \right) \Upsilon_{FM}, \quad (4.47)$$

where $k(r, v)$ is given by

$$k = \frac{2Ze\Psi}{mv} \left[\nu_\lambda \lambda_r \int_{l_{b10}}^{l_{b20}} B_0^{-1} \sqrt{1 - \lambda_r B_0} dl + \frac{\nu_v v^2}{2} (\partial_v \lambda_r)^2 \int_{l_{b10}}^{l_{b20}} \frac{1}{\sqrt{1 - \lambda_r B_0}} dl \right], \quad (4.48)$$

subindices r indicate that the corresponding quantity is evaluated at $\lambda = \lambda_r(r, v, \varphi'_0)$ and $\widehat{J_\varphi^{(1)}}$ is an approximation of $J_\varphi^{(1)}$ around λ_r . In particular, $\widehat{J_\varphi^{(1)}}$ is a function of v and ξ . We will see shortly why, in general, we cannot simply evaluate $J_\varphi^{(1)}$ at λ_r . The second term in (4.48) comes from the energy diffusion piece of the collision operator, which must be included because the coordinate across the layer (the coordinate in which g_{rl} varies fast), $\xi = \lambda - \lambda_r$, mixes v and λ . The collision frequency ν_v is given by

$$\nu_v(v) = \frac{3\sqrt{\pi} \chi \left(v \sqrt{m/(2T)} \right)}{2\tau_{ii} \left(v \sqrt{m/(2T)} \right)^3}. \quad (4.49)$$

In Calvo *et al.* (2017), the energy diffusion piece of the collision operator was incorrectly neglected. Note that none of the scalings derived in Calvo et al (2017) are affected by the inclusion of energy diffusion.

Using that $\partial_\lambda \partial_r J_r^{(0)} = O(B_0 v_t)$ and that $k(r, v) = O(\nu_\lambda B_0^{-2} R_0 \rho_*^{-1})$, and balancing the two terms on the left-hand side of (4.47), we deduce that g_{rl} is localized in a layer whose size in the coordinate ξ is

$$B_0 \Delta_{sb-p} \sim (\nu_*/\rho_*)^{1/3}. \quad (4.50)$$

Then, balancing the left- and right-hand sides of (4.47), we find that

$$g_{rl} \sim (B_0 \Delta_{sb-p})^{-1} F_M. \quad (4.51)$$

This resonant layer, via g_{rl} , is responsible for superbanana-plateau transport.

The solution outside the resonant layer is given by (4.30). Since g_0 diverges at λ_r , we remove the divergence so that we obtain a function g_0^{out} which is finite everywhere and asymptotically coincides with g_0 far from the resonant layer. Namely,

$$g_0^{\text{out}} = g_0 - \frac{1}{(\lambda - \lambda_r) \partial_\lambda \partial_r J_r^{(0)}} \left(\widetilde{J}_{B,r}^{(1)} + \widehat{J_\varphi^{(1)}} - \frac{1}{2\pi} \int_0^{2\pi} \widehat{J_\varphi^{(1)}} d\alpha \right) \Upsilon F_M, \quad (4.52)$$

where $\widetilde{J}_{B,r}^{(1)}$ is the quantity defined in (4.35) evaluated at λ_r .

In principle, both pieces, g_0^{out} and g_{rl} , contribute equally to the quasineutrality equation (although only g_{rl} contributes to radial transport). Hence, one needs to solve

$$\varphi^{(1)} = \frac{2\pi B_0}{en} \left(\frac{Z}{T} + \frac{1}{T_e} \right)^{-1} \left[\int_0^\infty dv \int_{B_0^{-1}, \max}^{B^{-1}} d\lambda \frac{v^3 g_0^{\text{out}}}{|v_{||}^{(0)}|} + \int_I dv \int_{K \Delta_{sb-p}} d\lambda \frac{v^3 g_{rl}}{|v_{||}^{(0)}|} \right], \quad (4.53)$$

with $K \gg 1$. An explicit, asymptotically correct expression for the quasineutrality equa-

tion is given by (see Calvo *et al.* (2017) for the details)

$$\begin{aligned}
\varphi^{(1)} = & \frac{2\pi B_0}{en} \left(\frac{Z}{T} + \frac{1}{T_e} \right)^{-1} \left\{ \int_0^\infty dv \int_{B_{0,\max}^{-1}}^{B^{-1}} d\lambda \frac{v^3}{|v_{||}^{(0)}|} g_0^{\text{out}} \right. \\
& + \int_I dv v^2 \int_{-\infty}^{\lambda_L(l)} d\lambda \frac{g_{rl}}{\sqrt{\lambda_r |\partial_l B_0(l_L)| (l - l_L) - (\lambda - \lambda_r) B_0(l_L)}} \\
& + \int_I dv v^2 \int_{-\infty}^{\lambda_R(l)} d\lambda \frac{g_{rl}}{\sqrt{\lambda_r |\partial_l B_0(l_R)| (l_R - l) - (\lambda - \lambda_r) B_0(l_R)}} \\
& + \int_I dv v^2 \left[\frac{1}{\sqrt{1 - \lambda_r B_0(l)}} - \frac{1}{\sqrt{\lambda_r |\partial_l B_0(l_L)| (l - l_L)}} \right. \\
& \left. \left. - \frac{1}{\sqrt{\lambda_r |\partial_l B_0(l_R)| (l_R - l)}} \right] \int_{-\infty}^\infty d\lambda g_{rl} \right\}, \tag{4.54}
\end{aligned}$$

where l_L and l_R denote the bounce points of the trajectory $\lambda = \lambda_r$,

$$\lambda_L(l) - \lambda_r = \frac{\lambda_r |\partial_l B_0(l_L)| (l - l_L)}{B_0(l_L)} \tag{4.55}$$

and

$$\lambda_R(l) - \lambda_r = \frac{\lambda_r |\partial_l B_0(l_R)| (l_R - l)}{B_0(l_R)}. \tag{4.56}$$

Expression (4.54) is useful in order to explain why we did not evaluate $J_\varphi^{(1)}$ at λ_r in equation (4.47). First, note that the first term in brackets in the fourth line of (4.54) diverges at $l = l_L$ and $l = l_R$. We distinguish two cases:

(i) If

$$\left| \frac{2Ze\varphi'_0}{mv^2 \lambda_r \partial_\lambda \partial_r B_0(\lambda_r)} \right| \gg \Delta_{\text{sb-p}}, \tag{4.57}$$

the dependence of λ_r on v is strong enough for the integral over v to smooth out the divergence of $1/\sqrt{1 - \lambda_r B_0(l)}$ at $l = l_L$ and $l = l_R$. Then,

$$\varphi^{(1)} \sim \frac{T}{e}. \tag{4.58}$$

In this case, $\widehat{J_\varphi^{(1)}}$ can be replaced by $J_{\varphi,r}^{(1)}$ in (4.47), where

$$J_{\varphi,r}^{(1)} = -\frac{2Ze}{mv} \int_{l_{b10}}^{l_{b20}} \frac{\varphi^{(1)}}{\sqrt{1 - \lambda_r B_0}} dl, \tag{4.59}$$

and the solution of (4.47) can be found analytically, with g_{rl} approaching a Dirac delta distribution when the collision frequency tends to zero. This gives the standard superbanana-plateau regime in which the radial neoclassical fluxes are strictly independent of the collisionality. This regime was treated in Shaing (2015) for tokamaks of finite aspect ratio with broken symmetry.

(ii) If

$$\left| \frac{2Ze\varphi'_0}{mv^2 \lambda_r \partial_\lambda \partial_r B_0(\lambda_r)} \right| \ll \Delta_{\text{sb-p}}, \tag{4.60}$$

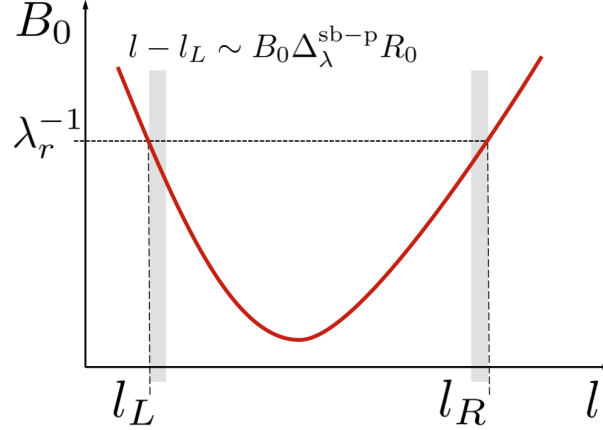


FIGURE 9. If (4.60) is satisfied, the resonant value λ_r is approximately independent of v . The accumulated effect of the resonance for all possible values of v produces a larger $\varphi^{(1)}$ in a neighborhood of the bounce points of the resonant trajectory, l_L and l_R .

then λ_r is approximately independent of v and no such smoothing happens. The effect of the accumulation of the resonances at the same λ_r for every v causes that, close to the bounce points of the resonant trajectory, the electrostatic potential become very large. Specifically, one finds that

$$\varphi^{(1)} \sim \begin{cases} (\nu_*/\rho_*)^{-1/6} T/e & |l - l_j| \sim B_0 \Delta_{\text{sb-p}} R_0 \\ T/e & |l - l_j| \gg B_0 \Delta_{\text{sb-p}} R_0, \end{cases} \quad (4.61)$$

where $j = L, R$ (see figure 9). This subregime of the superbanana-plateau regime was discovered in Calvo *et al.* (2017) and we will focus on it in the next subsection, devoted to illustrating it numerically. When (4.60) holds, the radial neoclassical fluxes depend logarithmically on collisionality. The estimation (4.50) for the size of the layer also incorporates logarithmic corrections.

Finally, we point out that, as clearly inferred from inspection of (4.47), g_{rl} has no definite parity under stellarator symmetry transformations, and neither does $\varphi^{(1)}$.

4.3.1. Superbanana-plateau regime in a large aspect ratio stellarator

We start by giving some estimates that are needed below. First, note that $\partial_\lambda \partial_r J_r^{(0)} \sim \epsilon^{-3/2} v_t B_{00}$. Second, observe that for large aspect ratio $\partial_v \lambda_r \sim \epsilon/(B_{00} v_t)$ so that the term proportional to ν_v in (4.48) can be neglected compared to the term proportional to ν_λ , giving $k \sim \epsilon^{3/2} \nu_\lambda B_{00}^{-2} R_0 \rho_*^{-1}$. Then, balancing the two terms on the left-hand side of the drift-kinetic equation (4.47), we find that, for $\epsilon \ll 1$,

$$B_{00} \Delta_{\text{sb-p}} \sim \epsilon \left(\frac{\nu_*}{\rho_*} \right)^{1/3}. \quad (4.62)$$

For convenience, define $g_{\text{rl}}[J_B^{(1)}]$ and $g_{\text{rl}}[J_\varphi^{(1)}]$ as the solutions of

$$\partial_\lambda \partial_r J_r^{(0)} \xi \partial_\alpha g_{\text{rl}}[J_B^{(1)}] + k \partial_\xi^2 g_{\text{rl}}[J_B^{(1)}] = \partial_\alpha J_{B,r}^{(1)} \Upsilon F_M \quad (4.63)$$

and

$$\partial_\lambda \partial_r J_r^{(0)} \xi \partial_\alpha g_{\text{rl}}[J_\varphi^{(1)}] + k \partial_\xi^2 g_{\text{rl}}[J_\varphi^{(1)}] = \partial_\alpha \widehat{J_\varphi^{(1)}} \Upsilon F_M, \quad (4.64)$$

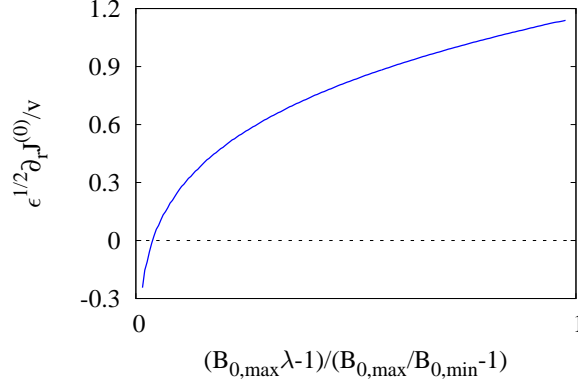


FIGURE 10. $\partial_r J^{(0)}$ as a function of λ in our model omnigeneous magnetic field, with $\epsilon = 1.1 \times 10^{-4}$ and $\varphi'_0 = 0$. The value of λ at which $\partial_r J^{(0)}$ vanishes determines the resonant value λ_r . Here, $(B_{0,\max} \lambda_r - 1) / (B_{0,\max} / B_{0,\min} - 1) = 0.04$.

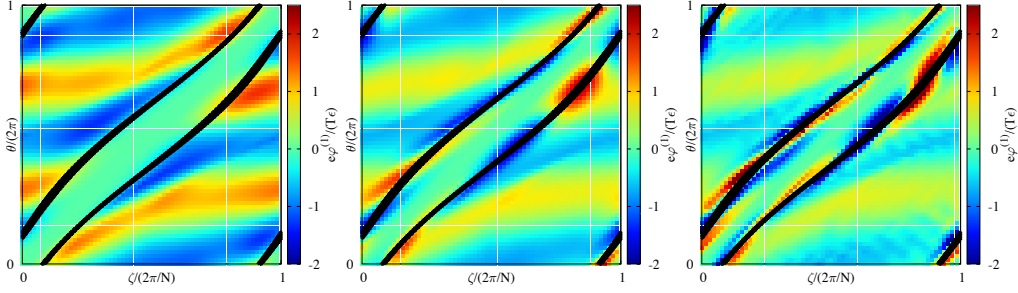


FIGURE 11. Contour plot of $\varphi^{(1)}$ for $\epsilon = 1.1 \times 10^{-4}$, $\varphi'_0 = 0$ and three values of the collisionality. From left to right, $\nu_* = 1.2 \times 10^{-12}$, $\nu_* = 1.3 \times 10^{-13}$, $\nu_* = 1.3 \times 10^{-14}$. The black lines are the two curves determined by the left and right bounce points of the resonant trajectory, l_L and l_R , respectively. When ν_* decreases, the increase of $\varphi^{(1)}$ around l_L and l_R , as predicted by (4.67), is confirmed. The color scale has been kept constant in the three figures, so that the increase in $\varphi^{(1)}$ becomes clearer; that is, in the center and right figures, $e|\varphi^{(1)}|/(T\epsilon)$ reaches larger values than the largest one indicated in the color scale bar.

respectively. Of course, $g_{rl} = g_{rl}[J_B^{(1)}] + g_{rl}[J_\varphi^{(1)}]$. Then,

$$g_{rl}[J_B^{(1)}] \sim \left(\frac{\nu_*}{\rho_*} \right)^{-1/3} \frac{n}{v_t^3} \quad (4.65)$$

and

$$g_{rl}[J_\varphi^{(1)}] \sim \epsilon^{-1/2} \left(\frac{\nu_*}{\rho_*} \right)^{-1/3} \frac{J_\varphi^{(1)}}{v_t R_0} \frac{n}{v_t^3}. \quad (4.66)$$

One can deal with the quasineutrality equation (4.54) by employing again the procedure followed after (4.17) and also in subsection 4.2.2. The result is that

$$\varphi^{(1)} \sim \begin{cases} (\nu_*/\rho_*)^{-1/6} \epsilon T/e & |l - l_j| \sim B_{00} \Delta_{sb-p} R_0 \\ \epsilon T/e & |l - l_j| \gg B_{00} \Delta_{sb-p} R_0. \end{cases} \quad (4.67)$$

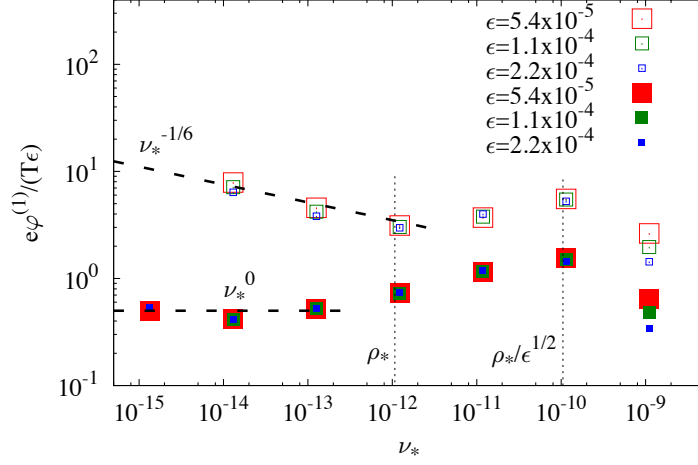


FIGURE 12. Size of $\varphi^{(1)}$ as a function of ν_* and ϵ . Here, $\varphi'_0 = 0$. The two scalings given in equation (4.67) are checked. Full squares give the size of $\varphi^{(1)}$ at generic points, $|l - l_j| \gg B_{00}\Delta_{sb-p}R_0$, whereas empty squares give the size of $\varphi^{(1)}$ at a point that is very close to a bounce point of the resonant trajectory, $|l - l_j| \sim B_{00}\Delta_{sb-p}R_0$ (that is, empty squares give approximately the maximum of $\varphi^{(1)}$ on the flux surface).

Let us check numerically the scalings of this subsection. First, in figure 10, we show the dependence of $\partial_r J^{(0)}$ on λ for $\varphi'_0 = 0$ in our model magnetic configuration and we give, in particular, the location in phase space of the resonant value λ_r . In figure 11, contour plots of $\varphi^{(1)}$ are shown for three different values of the collisionality, so that one can see how $\varphi^{(1)}$ becomes larger and larger around l_L and l_R as the collisionality decreases. Figure 12 provides a precise numerical check of the two scalings given in (4.67).

5. Conclusions

The component of the neoclassical electrostatic potential that is non-constant on flux surfaces, $\tilde{\varphi}$ (equivalently, the component of the electric field that is tangential to the surface), has been proven to have an important impact on stellarator radial impurity transport (García-Regaña *et al.* 2013), triggering interest in the correct calculation of the tangential electric field, which has often been neglected in stellarator neoclassical theory. On the numerical side, remarkable effort has been made during recent years (see García-Regaña *et al.* (2017) and references therein). In this article, we have studied analytically the scaling of $\tilde{\varphi}$ with collisionality and aspect ratio, and its structure on the flux surface.

The tangential electric field can be remarkably large when the collisionality is low enough for the tangential drifts to count in the drift-kinetic equation and especially when the tangential magnetic drift is non-negligible. If the collisionality and the radial electric field are such that the tangential magnetic drift cannot be dropped, the neoclassical equations can be kept linear and radially local only if the stellarator is sufficiently optimized (Calvo *et al.* 2017); i.e. if the magnetic configuration is sufficiently close to

Parameter range	Size of $e\varphi^{(1)}/T$	Behavior under stellarator symmetry	Radial transport regime
Large radial electric field, $ \varphi'_0 \sim \epsilon^{-1}T/(eR_0)$			
$\epsilon^{-1}\rho_* \ll \nu_* \ll \epsilon^{3/2}$	$\epsilon^{1/2}\rho_*/\nu_*$	Antisymmetric	$1/\nu$
$\nu_* \ll \epsilon^{-1}\rho_*$	$\epsilon^{3/2}$	Symmetric	$\sqrt{\nu}$
Small radial electric field, $ \varphi'_0 \lesssim T/(eR_0)$			
$\epsilon^{-1/2}\rho_* \ll \nu_* \ll \epsilon^{3/2}$	$\epsilon^{1/2}\rho_*/\nu_*$	Antisymmetric	$1/\nu$
$\rho_* \ll \nu_* \ll \epsilon^{-1/2}\rho_*$	ϵ	Symmetric	$1/\nu$
$\nu_* \ll \rho_*$ ($\partial_r J^{(0)}$ has no zeros)	ϵ	Symmetric	$\sqrt{\nu}$
$\nu_* \ll \rho_*$ ($\partial_r J^{(0)}$ has zeros)	ϵ , at generic points $\epsilon(\nu_*/\rho_*)^{-1/6}$, at special points, if any	No defined symmetry	Superbanana-plateau

TABLE 1. Asymptotic regimes for $\varphi^{(1)}$

omnigeneity (Cary & Shasharina 1997; Parra *et al.* 2015). This is why we have conducted our study in the framework of a stellarator that is close to being omnigeneous, employing the techniques developed in Calvo *et al.* (2017), where a small parameter δ exists that gives the size of the deviation from perfect omnigeneity. Throughout the paper, and employing some results of Calvo *et al.* (2017), we discuss the calculation of the tangential electric field for collisionality values that cover the $1/\nu$, $\sqrt{\nu}$ and superbanana-plateau regimes, and in each of them provide its size, scaling with collisionality, aspect ratio and δ , and behavior under stellarator symmetry transformations. In the treatment presented in Calvo *et al.* (2017) no assumption was made about the aspect ratio of the stellarator. Here, we have investigated how the results are modified when, apart from the δ expansion, one takes a subsidiary expansion in large aspect ratio. We have found new regimes that did not appear in tight aspect ratio devices. In particular, we have deduced that the maximum size admitted for $\tilde{\varphi} := \delta\varphi^{(1)}$ by the neoclassical equations is given by $\varphi^{(1)} \sim \epsilon T/e$, except at some special points where it can be larger. Table 1 summarizes the analytical results, providing the scaling with collisionality and aspect ratio in each regime. The notation is explained in Sections 2 and 4.

The analytical results for each asymptotic regime have been verified and illustrated by numerical calculations of the code **KNOSOS**, that solves the equations derived in Calvo *et al.* (2017) for stellarators close to omnigeneity, the same set of equations that are the subject of study of this paper. In figure 3, choosing realistic values for a stellarator reactor plasma, we have represented the size of $\varphi^{(1)}$ as a function of the collisionality, showing the different regimes in a single figure.

Finally, we comment on the expected effect of $\tilde{\varphi}$ on the radial neoclassical transport

of the main ions. This effect is negligible compared to the transport due to B_1 except in regimes where $\tilde{\varphi}$ reaches its maximum size, given by $\varphi^{(1)} \sim \epsilon T/e$ (see Table 1). In principle, in such regimes, the contributions of B_1 and $\tilde{\varphi}$ to the main ion neoclassical fluxes can be comparable. In practice, however, the maximum size reached by $\tilde{\varphi}$ is somewhat smaller. Obtaining $\varphi^{(1)} \sim \epsilon T/e$ seems to require density profile gradients $|n'/n| \sim (\epsilon R_0)^{-1}$, like the ones employed in this paper. If one takes a smaller density profile gradient and $|T'/T| \sim (\epsilon R_0)^{-1}$ (a situation that is more common in stellarators), the scaling of $\tilde{\varphi}$ does not change but the actual value is smaller, due to the different way in which the density and temperature profiles enter the source term of the drift-kinetic equation.

Appendix A. Application of the Abel transform to integrals over trapped trajectories

We give a useful inversion formula that interchanges the coordinates l and λ . In this appendix, the coordinates r , α and v are irrelevant, and we omit them.

For any function $f(l)$, we define $F(\lambda)$ as the following integral over the trapped trajectory determined by $\lambda \in [B_{0,\max}^{-1}, B_{0,\min}^{-1}]$,

$$F(\lambda) := \int_{l_{b_{10}}(\lambda)}^{l_{b_{20}}(\lambda)} \frac{f(l)}{\sqrt{1 - \lambda B_0(l)}} dl. \quad (\text{A } 1)$$

Then, given a value of the magnetic field $\hat{B} \in [B_{0,\min}, B_{0,\max}]$, we have

$$\left. \frac{f}{|\partial_l B_0|} \right|_{l_{b_{20}}(\hat{B}^{-1})} + \left. \frac{f}{|\partial_l B_0|} \right|_{l_{b_{10}}(\hat{B}^{-1})} = -\frac{1}{\pi \hat{B}} \int_{\hat{B}^{-1}}^{B_{0,\min}^{-1}} \frac{dF}{d\lambda} \frac{1}{\sqrt{\lambda \hat{B} - 1}} d\lambda, \quad (\text{A } 2)$$

which can be proven by direct check. This formula can be viewed as a particularization of the Abel transform (Abel 1826).

For the sake of the application of the inversion formula in the main text of this article, we point out the following property, which is immediately derived from (A 2): if $f(l)$ is such that $B_0(l_1) = B_0(l_2) \Rightarrow f(l_1) = f(l_2)$, then

$$F(\lambda) = 0, \text{ for every } \lambda \Rightarrow f(l) = 0, \text{ for every } l. \quad (\text{A } 3)$$

The authors would like to thank an anonymous referee for pointing out that, in general, the energy diffusion piece of the collision operator cannot be neglected in equation (4.47). This work has been carried out within the framework of the EUROfusion Consortium and has received funding from the Euratom research and training programme 2014-2018 under grant agreement No 633053. The views and opinions expressed herein do not necessarily reflect those of the European Commission. This research was supported in part by grant ENE2015-70142-P, Ministerio de Economía y Competitividad, Spain.

REFERENCES

- ABEL, N. H. 1826 Auflösen einer mechanischen Aufgabe. *J. Reine Angew. Math.* **1**, 153.
 ALONSO, J. A., VELASCO, J. L., CALVO, I., ESTRADA, T., FONTDECABA, J. M., GARCÍA-REGAÑA, J. M., GEIGER, J., LANDREMAN, M., MCCARTHY, K. J., MEDINA, F., VAN MILLIGEN, B. PH., OCHANDO, M. A., PARRA, F. I., THE TJ-II TEAM & THE W7-X

- TEAM 2016 Parallel impurity dynamics in the TJ-II stellarator. *Plasma Phys. Control. Fusion* **58**, 074009.
- ARÉVALO, J., ALONSO, J. A., MCCARTHY, K. J., VELASCO, J. L., GARCÍA-REGAÑA, J. M. & LANDREMAN, M. 2014 Compressible impurity flow in the TJ-II stellarator. *Nucl. Fusion* **54**, 013008.
- BEIDLER, C. D., ALLMAIER, K., ISAEV, M. YU., KASILOV, S. V., KERNBICHLER, W., LEITOLD, G. O., MAASSBERG, H., MIKKELSEN, D. R., MURAKAMI, S., SCHMIDT, M., SPONG, D. A., TRIBALDOS, V. AND WAKASA, A. 2011 Benchmarking of the mono-energetic transport coefficients—results from the International Collaboration on Neoclassical Transport in Stellarators (ICNTS). *Nucl. Fusion* **51**, 076001.
- BOOZER, A. H. 1981 Plasma equilibrium with rational magnetic surfaces. *Phys. Fluids* **24**, 1999.
- BURHENN, R., FENG Y., IDA, K., MAASSBERG, H., MCCARTHY, K. J., KALININA, D., KOBAYASHI, M., MORITA, S., NAKAMURA, Y., NOZATO, H., OKAMURA, S., SUDO, S., SUZUKI, C., TAMURA, N., WELLER, A., YOSHINUMA, M. & ZURRO B. 2009 On impurity handling in high performance stellarator/heliotron plasmas. *Nucl. Fusion* **49**, 065005.
- CALVO, I., PARRA, F. I., VELASCO, J. L. & ALONSO, J. A. 2013 Stellarators close to quasisymmetry. *Plasma Phys. Control. Fusion* **55**, 125014.
- CALVO, I., PARRA, F. I., ALONSO, J. A. & VELASCO, J. L. 2014 Optimizing stellarators for large flows. *Plasma Phys. Control. Fusion* **56**, 094003.
- CALVO, I., PARRA, F. I., VELASCO, J. L. & ALONSO, J. A. 2015 Flow damping in stellarators close to quasisymmetry. *Plasma Phys. Control. Fusion* **57**, 014014.
- CALVO, I., PARRA, F. I., VELASCO, J. L. & ALONSO, J. A. 2017 The effect of tangential drifts on neoclassical transport in stellarators close to omnigenity. *Plasma Phys. Control. Fusion* **59**, 055014.
- CALVO, I., PARRA, F. I., VELASCO, J. L., ALONSO, J. A. & GARCÍA-REGAÑA, J. M. Stellarator impurity flux driven by electric fields tangent to magnetic surfaces. [arXiv:1803.05691](#).
- CARY, J. R. & SHASHARINA, S. G. 1997 Omnigenity and quasihelicity in helical plasma confinement systems. *Phys. Plasmas* **4**, 3323.
- DEWAR, R. L. & HUDSON, S. R. 1998 Stellarator symmetry. *Physica D: Nonlinear Phenomena* **112**, 275.
- GALEEV, A. A. & SAGDEEV, R. Z. 1979 Theory of neoclassical diffusion *Reviews of Plasma Physics*, vol 7, p 257 ed Leontovich, M. A. (New York: Consultants Bureau).
- GARCÍA-REGAÑA, J. M., KLEIBER, R., BEIDLER, C. D., TURKIN, Y., MAASSBERG, H. & HELANDER, P. 2013 On neoclassical impurity transport in stellarator geometry. *Plasma Phys. Control. Fusion* **55**, 074008.
- GARCÍA-REGAÑA, J. M., BEIDLER, C. D., KLEIBER, R., HELANDER, P., MOLLÉN, A., ALONSO, J. A., LANDREMAN, M., MAASSBERG, H., SMITH, H. M., TURKIN, Y. & VELASCO, J. L. 2017 Electrostatic potential variation on the flux surface and its impact on impurity transport. *Nucl. Fusion* **57**, 056004.
- GARCÍA-REGAÑA, J. M., ESTRADA, T., CALVO, I., VELASCO, J. L., ALONSO, J. A., CARRALERO, D., KLEIBER, R., LANDREMAN, M., MOLLÉN, A., SÁNCHEZ, E., SLABY, C., TJ-II TEAM & W7-X TEAM. On-surface potential and radial electric field variations in electron root stellarator plasmas. [arXiv:1804.10424](#).
- HALL, L. S. & MCNAMARA, B. 1975 Three-dimensional equilibrium of the anisotropic, finite-pressure guiding-center plasma: Theory of the magnetic plasma. *Phys. Fluids* **18**, 552.
- HAZELTINE, R. D. 1973 Recursive derivation of drift-kinetic equation. *Plasma Phys.* **15**, 77.
- HELANDER, P. & SIGMAR, D. J. 2002 Collisional Transport in Magnetized Plasmas (Cambridge Monographs on Plasma Physics) ed Haines M G et al (Cambridge, UK: Cambridge University Press)
- HELANDER, P. & NÜHRENBURG, J. 2009 Bootstrap current and neoclassical transport in quasi-isodynamic stellarators. *Plasma Phys. Control. Fusion* **51**, 055004.
- HELANDER, P., NEWTON, S. L., MOLLÉN, A. & SMITH, H. M. 2017 Impurity transport in a mixed-collisionality stellarator plasma. *Phys. Rev. Lett.* **118**, 155002.
- HO, D. D. M. & KULSRUD, R. M. 1987 Neoclassical transport in stellarators. *Phys. Fluids* **30**, 442.
- IDA, K., YOSHINUMA, M., OSAKABE, M., NAGAOKA, K., YOKOYAMA, M., FUNABA, H.,

- SUZUKI, C., IDO, T., SHIMIZU, A., MURAKAMI, I., TAMURA, N., KASAHARA, H., TAKEIRI, Y., IKEDA, K., TSUMORI, K., KANEKO, O., MORITA, S., GOTO, M., TANAKA, K., NARIHARA, K., MINAMI, T. & YAMADA, I. 2009 Observation of an impurity hole in a plasma with an ion internal transport barrier in the large helical device. *Phys. Plasmas* **16**, 056111.
- KLINGER, T., ALONSO, A., BOZHENKOV, S., BURHENN, R., DINKLAGE, A., FUCHERT, G., GEIGER, J., GRULKE, O., LANGENBERG, A., HIRSCH, M., KOCSIS, G., KNAUER, J., KRÄMER-FLECKEN, A., LAQUA, H., LAZERSON, S., LANDREMAN, M., MAASSBERG, H., MARSEN, S., OTTE, M., PABLANT, N., PASCH, E., RAHBARNIA, K., STANGE, T., SZEPESI, T., THOMSEN, H., TRAVERSO, P., VELASCO, J. L., WAUTERS, T., WEIR, G., WINDISCH, T. AND THE WENDELSTEIN 7-X TEAM 2017 Performance and properties of the first plasmas of Wendelstein 7-X. *Plasma Phys. Control. Fusion* **59**, 014018.
- KORNILOV, V., KLEIBER, R. & HATZKY, R. 2005 Gyrokinetic global electrostatic ion-temperature-gradient modes in finite β equilibria of Wendelstein 7-X. *Nucl. Fusion* **45**, 238.
- LANDREMAN, M. & CATTO, P. J. 2012 Omnigenity as generalized quasisymmetry. *Phys. Plasmas* **19**, 056103.
- LANDREMAN, M., SMITH, H. M., MOLLÉN, A. & HELANDER, P. 2014 Comparison of particle trajectories and collision operators for collisional transport in nonaxisymmetric plasmas. *Phys. Plasmas* **21**, 042503.
- MATSUOKA, S., SATAKE, S., KANNO, R. & SUGAMA, H. 2015 Effects of magnetic drift tangential to magnetic surfaces on neoclassical transport in non-axisymmetric plasmas. *Phys. Plasmas* **22**, 072511.
- MCCORMICK, K., GRIGULL, P., BURHENN, R., BRAKEL, R., EHMLER, H., FENG, Y., GADELMEIER, F., GIANNONE, L., HILDEBRANDT, D., HIRSCH, M., JAENICKE, R., KISSLINGER, J., KLINGER, T., KLOSE, S., KNAUER, J. P., KÖNIG, R., KÜHNER, G., LAQUA, H. P., NAUJOKS, D., NIEDERMEYER, H., PASCH, E., RAMASUBRAMANIAN, N., RUST, N., SARDEI, F., WAGNER, F., WELLER, A., WENZEL, U. & WERNER, A. 2002 New advanced operational regime on the W7-AS stellarator. *Phys. Rev. Lett.* **89**, 015001.
- MOLLÉN, A., LANDREMAN, M., SMITH, H. M., GARCÍA-REGAÑA, J. M., & NUNAMI, M. 2018 Flux-surface variations of the electrostatic potential in stellarators: impact on the radial electric field and neoclassical impurity transport. *Plasma Phys. Control. Fusion* **60**, 084001.
- MYNICK, H. E. 1984 Calculation of the poloidal ambipolar field in a stellarator and its effect on transport. *Phys. Fluids* **27**, 2086.
- PARRA, F. I. & CALVO, I. 2011 Phase-space Lagrangian derivation of electrostatic gyrokinetics in general geometry. *Plasma Phys. Control. Fusion* **53**, 045001.
- PARRA, F. I., CALVO, I., HELANDER, P. AND LANDREMAN, M. 2015 Less constrained omnigenous stellarators. *Nucl. Fusion* **55**, 033005.
- PAUL, E. J., LANDREMAN, M., POLI, F. M., SPONG, D. A., SMITH, H. M. & DORLAND, W. 2017 Rotation and neoclassical ripple transport in ITER. *Nucl. Fusion* **57**, 116044.
- PEDROSA, M. A., ALONSO, J. A., GARCÍA-REGAÑA, J. M., HIDALGO, C., VELASCO, J. L., CALVO, I., KLEIBER, R., SILVA, C. & HELANDER, P. 2015 Electrostatic potential variations along flux surfaces in stellarators. *Nucl. Fusion* **55**, 052001.
- SHAING, K. C. 2015 Superbanana and superbanana plateau transport in finite aspect ratio tokamaks with broken symmetry. *J. Plasma Physics* **81**, 905810203.
- VELASCO, J. L., CALVO, I., SATAKE, S., ALONSO, J. A., NUNAMI, M., YOKOYAMA, M., SATO, M., ESTRADA, T., FONTDECABA, J. M., LINIERS, M., MCCARTHY, K. J., MEDINA, F., VAN MILLIGEN, B. PH., OCHANDO, M., PARRA F. I., SUGAMA, H., ZHEZHERA, A., THE LHD EXPERIMENTAL TEAM & THE TJ-II TEAM 2017 Moderation of neoclassical impurity accumulation in high temperature plasmas of helical devices. *Nucl. Fusion* **57**, 016016.
- VELASCO, J. L., CALVO, I., GARCÍA-REGAÑA, J. M., PARRA, F. I., SATAKE, S., ALONSO, J. A. & THE LHD TEAM 2018 Large tangential electric fields in plasmas close to temperature screening. *Plasma Phys. Control. Fusion* **60**, 074004.